Chapter 11

Influence of Cloud Microphysics and Radiation on Tropical Cyclone Structure and Motion

ROBERT G. FOVELL,* YIZHE PEGGY BU,* KRISTEN L. CORBOSIERO,+ WEN-WEN TUNG,#
YANG CAO,* HUNG-CHI KUO,@ LI-HUAN HSU,** AND HUI SU++

* *Department of Atmospheric and Oceanic Sciences, University of California, Los Angeles, Los Angeles, California*
+ *Department of Atmospheric and Environmental Sciences, University at Albany, State University of New York, Albany, New York*
# *Department of Earth, Atmospheric and Planetary Sciences, Purdue University, West Lafayette, Indiana*
@ *Department of Atmospheric Sciences, National Taiwan University, Taipei, Taiwan*
** *Taiwan Typhoon Flood and Research Institute, Taipei, Taiwan*
++ *Jet Propulsion Laboratory, California Institute of Technology, Pasadena, California*

ABSTRACT

The authors survey a series of modeling studies that have examined the influences that cloud microphysical processes can have on tropical cyclone (TC) motion, the strength and breadth of the wind field, inner-core diabatic heating asymmetries, outer-core convective activity, and the characteristics of the TC anvil cloud. These characteristics are sensitive to the microphysical parameterization (MP) in large part owing to the cloud-radiative forcing (CRF), the interaction of hydrometeors with radiation. The most influential component of CRF is that due to absorption and emission of longwave radiation in the anvil, which via gentle lifting directly encourages the more extensive convective activity that then leads to a radial expansion of the TC wind field. On a curved Earth, the magnitude of the outer winds helps determine the speed and direction of TC motion via the beta drift. CRF also influences TC motion by determining how convective asymmetries develop in the TC inner core. Further improvements in TC forecasting may require improved understanding and representation of cloud-radiative processes in operational models, and more comprehensive comparisons with observations are clearly needed.

1. Introduction

Professor Michio Yanai's life-long love of weather started in middle school, when he joined the school's meteorology club (*otenkikai*). He and his fellow ''meteorology boys'' were particularly interested in the tropical cyclones (TCs) that frequently visited Japan during the autumn months, going so far as issuing their own weather warnings, making their own measurements, and conducting their own damage surveys. After graduating from the University of Tokyo with a degree in geophysics, he stayed on for graduate studies in meteorology. His master's thesis [published as Yanai (1958)] focused on a decaying typhoon, and this was soon followed by a series of seminal papers on TC genesis that appeared in rapid succession, including Yanai (1961a,b), Yanai (1963a,b), and Yanai (1964).

Subsequently, Professor Yanai shifted his research focus to different areas, which are represented by other papers in this volume, but he never relinquished a keen interest in TCs. He was concerned about their societal impacts, historical variations, and even their nomenclature. In his last years, he frequently returned to the subject of Cyclone Nargis (2008), which brought enormous devastation to Myanmar. Indeed, just a week before his untimely passing in October 2010, Professor Yanai was organizing yet another issue of his University of California, Los Angeles Tropical Meteorology Newsletter, started in 1996 and distributed via e-mail, dedicated to summarizing the

Corresponding author address: Prof. Robert Fovell, UCLA Atmospheric and Oceanic Sciences, 405 Hilgard Ave., Los Angeles, CA 90096-1565.
E-mail: rfovell@ucla.edu

DOI: 10.1175/AMSMONOGRAPHS-D-15-0006.1

© 2016 American Meteorological Society

TABLE 11-1. Models employed in the semi-idealized experiments.

Paper No.	Study	Model/version	No. of domains	Finest resolution (km)	Remarks
1	Fovell and Su (2007)	ARW 2.2	3	3	—
2	Fovell et al. (2009)	ARW 2.2.1	3	3	—
3–4	Fovell et al. (2010a,b)	ARW 2.2.1	1	4	—
5	Cao et al. (2011)	ARW 3.0	2	3	Moving nest
6	Hsu et al. (2013)	ARW 3.1.1	1	5	Water mountain
7	Bu et al. (2014)	HWRF pre-2013	3	3	Two moving nests
		CM1	1	5	Axisymmetric
—	This review	ARW 3.2	1	4	"Augmented P3"
—	This review	MPAS 2.0	1	25	Global, 92 to 25 km

ongoing Nargis research. In May 2005, Professor Yanai published a review of the origins of the words "typhoon," "tai-feng," and "tai-fu," which was cowritten with his last doctoral student, Professor Chih-wen Hung, and the first author, Robert G. Fovell.

The first author's interest in TCs commenced in the summer of 2004 with the release of version 2.0 of the Weather Research and Forecasting (WRF) Model's Advanced Research WRF (ARW) core. He decided to familiarize himself with this new, more powerful ARW system by simulating TCs in real time,[1] and the 2004 season proved compelling, with four major hurricanes striking in or very near Florida and a historically large number of typhoons making landfall at Japan. He soon noticed that the cloud microphysics parameterization (MP), which controls the evolution of condensed water, could exert a material impact on storm track. A literature survey revealed relatively little understanding of the role of cloud processes on TC motion, and Professor Yanai provided critical encouragement for this research with his knowledge, insight, and enthusiasm.

This review summarizes the findings of seven papers (see Table 11-1) produced by the first author and his collaborators concerning cloud microphysics and their direct and indirect influences on TC motion and structure. Fovell and Su [2007, hereinafter P1 (for paper 1)] conducted a physics ensemble (consisting of MPs and cumulus parameterizations) for Hurricane Rita (2005). They also introduced the "semi-idealized" model framework employed in our subsequent work, which utilizes the "real-data" versions of models such as WRF and configurations similar to those implemented in operations. However, these models are dramatically simplified with respect to initialization, with a guiding philosophy that can be summarized by a famous dictum attributed to Albert Einstein: "make things as simple as possible, but not simpler." Fovell et al. (2009, hereinafter P2) demonstrated that varying microphysical assumptions resulted in different wind profiles in the outer core region (roughly 100–300 km from the eye), which contribute to distinct motions owing to the "beta drift" (see section 4a) that directly influences track. P2 further showed that track sensitivity was at least indirectly tied to particle terminal velocities.

Fovell et al. (2010b, hereinafter P3) introduced yet another simplification: they prevented hydrometeors from affecting longwave (LW) and shortwave (SW) radiation, effectively rendering clouds transparent. Track variation with respect to MP virtually disappeared, which demonstrated that the interplay of hydrometeors with radiation—which we term cloud-radiative forcing (CRF)—was a distinguishing factor among microphysics schemes. The interaction between condensed water and radiation is species dependent, and the MPs that generate more radiatively active particles also developed more radially extensive convective activity, different structural asymmetries with respect to diabatic forcing, and broader outer wind profiles. Fovell et al. (2010a, hereinafter P4) proposed that the cloud-top cooling and within-cloud warming resulting from CRF combined to help the anvil spread radially outward and thereby seeded the (normally dry) far environment, making it more favorable for the subsequent development of convection.

Naturally, microphysics alone cannot completely determine how a TC behaves. Cao et al. (2011, hereinafter P5) demonstrated that storm track and structure are both sensitive to the manner of TC initialization, and Hsu et al. (2013, hereinafter P6) showed how diabatic heating forced by flow over topography could explain speed variations of typhoons approaching and crossing an island like Taiwan. P4's explanation for outer region convective activity was finally assessed in Bu et al. (2014, hereinafter P7) and was determined to be insufficient to explain why CRF results in wider tropical cyclones. Their analysis identified LW absorption within the cloud anvil as the principal agent for

[1] Professor Fovell selected TCs because they seemed so much "simpler" than squall lines, which had been the principal focus of his research up to that time!

storm expansion, which potentially contributes to substantial track discrepancies.

The structure of this paper is as follows: The models employed in the experiments referenced herein are presented in section 2. Section 3 provides some cursory background information on cloud microphysics and radiative processes. The main findings are presented in section 4, and the final part of the paper summarizes this review.

2. Description of models and experiments

Studies P1–P7 have made use of different modeling systems in a variety of configurations and versions (see Table 11-1). This suite has included the WRF Model's ARW (Skamarock et al. 2007) and Nonhydrostatic Mesoscale Model (NMM) cores—the latter in its Hurricane WRF (HWRF) form (Gopalakrishnan et al. 2012)—and the Bryan Cloud Model 1 (CM1; Bryan and Fritsch 2002). For this review, additional experiments utilizing the above models as well as the global Model for Prediction across Scales (MPAS; Skamarock et al. 2012) have been made. All but CM1 started as ''real-data'' versions that were rendered semi-idealized by removing all land and setting the aquaplanet surface temperature at a uniform 29°C. These models are initialized with a horizontally homogeneous base state constructed from a single sounding that represents variants of Jordan's (1958) hurricane season composite. This approach facilitates analyses while retaining the dynamical frameworks that might be employed in operational settings.

The semi-idealized framework introduced in P1 used ARW v.2.2 with three telescoping and temporally fixed Mercator-projected domains with the highest horizontal resolution being 3 km. Model physics held fixed in those experiments included the Yonsei University (YSU; Hong et al. 2006) planetary boundary layer scheme, and the Dudhia (1989) SW and RRTM (Rapid Radiative Transfer Model; Mlawer et al. 1997) LW radiation parameterizations. Subsequent studies included alterations to the model version, domain width, depth, setup (including the incorporation of moving nests), and map projection (to Lambert conformal), as well as the horizontal and vertical resolutions. Adjustments were also made to the initial sounding and the model physics employed in the control configurations including, especially, new and improved radiation and microphysics schemes.

Many of our experiments have made use of a ''bubble'' initialization, in which a tropical cyclone is established over a 24-h period following the insertion of a synoptic-scale positive buoyancy perturbation at 20°N latitude into the otherwise horizontally homogeneous (and typically calm) base state. A convective parameterization is employed for the first 24 h at which time it is usually deactivated, depending on the domain setup and resolution. This technique can create a coherent cyclonic vortex of roughly tropical storm strength (with respect to the 10-m wind according to the Saffir–Simpson scale) in the first day. At that time, the microphysics parameterization is switched on (if it was not already active from the initial time). P5 contrasted this initialization, which was directly inspired by Hill and Lackmann (2009), with the customary technique of employing a ''bogus'' vortex of specified strength and structure.

The ARW simulations made expressly for this review used the configuration employed in P3, which consisted of a single 2700 km^2 domain with 4-km horizontal resolution but were made with version 3.2. Those experiments adopted the RRTM LW and Dudhia SW schemes. Along with P7's HWRF simulations, our MPAS runs employed RRTMG[2] for both longwave and shortwave.[3] Other radiation schemes used include Goddard (in CM1 for P7; Chou and Suarez 1994), HWRF's version of the GFDL parameterization (in P7; see also Gopalakrishnan et al. 2012), and CAM (Collins et al. 2006) and Fu–Liou–Gu (Fu and Liou 1993; Gu et al. 2010, 2011) in ARW (not shown). Finally, the CM1 model is employed solely in its axisymmetric configuration, with moist and dry simulations as described in P7. This model is used to test hypotheses relating to the influence of microphysics and cloud-radiative forcing on TCs.

This review combines results from these various experiments, using different models, configurations, and simulation strategies, because we are emphasizing the findings that are common to all studies. For example, we have found that, independent of the model or resolution employed, CRF invariably encourages the development of stronger winds in the TC's outer core region, as long as the MP schemes generate sufficient cloud ice and snow. Our first CRF experiment, made with ARW, suggested that TCs with transparent clouds were systematically more intense; however, this result was not found to be robust after simulations from other models such as HWRF, CM1, and MPAS were examined. As a consequence, TC intensity is largely ignored in this review, and remains an issue for further study.

[2] Rapid Radiative Transfer Model for general circulation models (Iacono et al. 2008).

[3] The P7 study used code provided by Greg Thompson to provide particle size information to the RRTMG radiation scheme. This improvement had little effect on the results, and is not employed herein. See P7 for further information.

3. Background

This section provides a brief background on some relevant aspects of cloud microphysics and cloud-radiative feedback. More comprehensive information is available in texts such as Liou (2002), Stensrud (2007), and Straka (2009), among others.

a. Cloud microphysics

Cloud microphysics comprises the processes that control the creation, evolution, and destruction of condensed water. The microphysical parameterizations that numerical models employ to handle these processes range from very simple to enormously complex. Condensed water particles come in a variety of basic species and sizes, and even in small volumes are far too numerous to individually track. Therefore, MPs have been developed that are either of the spectral or bulk varieties. In spectral (bin) microphysics the particle size distribution (PSD) is partitioned into discrete bins, and the evolution of particles through these partitions is modeled, which is usually a very expensive undertaking.

As a consequence, the vast majority of models employ bulk schemes in which the PSD for each species is specified separately. One of the earliest bulk MPs, the Kessler (1969) scheme, considered only "warm rain" processes involving cloud droplets and rainwater. Cloud droplets were presumed to be monodispersed (of constant size) and sufficiently small to be free-floating relative to still air. Raindrops were represented by an exponential size distribution (Fig. 11-1) characterized by an intercept (N_0) and a slope (λ), so that N_D, the number of drops of diameter D, is given by

$$N_D = N_0 e^{-\lambda D}. \tag{11-1}$$

This originated with the pioneering study of Marshall and Palmer (1948), who found that, except for the very smallest drop diameters, there was an exponential decrease in the number of rain drops collected as the diameter increased.

The total number of particles, N, is determined by integrating (11-1) over all possible drop sizes, which yields

$$N = \frac{N_0}{\lambda}.$$

If the drop is spherical, individual raindrops of diameter D have mass $M_D = \rho_l(\pi/6)D^3$, where ρ_l is the density of liquid water. The area under the line depicted in Fig. 11-1 is related to the total rainwater content in the model's grid volume, ρq_r, where ρ is the air density and q_r is the rainwater mixing ratio in kilograms of liquid per kilogram of air, which is presumed to be spread equally through the grid volume. Integrating over all drop sizes results in a relationship between the slope and intercept given by

$$\lambda = \left(\frac{\rho_l N_0 \pi}{\rho q_r}\right)^{1/4}. \tag{11-2}$$

The bulk terminal velocity applied to all raindrops in the volume is computed similarly, by taking the equation for a single drop of diameter D and integrating over all diameters.

"Single-moment" bulk MPs generally have fixed either N_0 or λ. While fixing the intercept is more common,[4] holding either constant is problematic. Constant N_0 means that the slope becomes more horizontal as the rainwater content increases, which implies that incremental increases in rain content come from assumed growth in the relatively larger drops within the PSD. "Double-moment" schemes relieve this constraint by prognosing the total mass and number of drops separately, which is more realistic but increases the computational complexity. More modern schemes have addressed some of the inherent limitations of particle size distributions based on (11-1) by adopting other functional shapes, such as the "gamma" distribution (cf. Willis 1984; Ziegler 1985; Seifert and Beheng 2006).

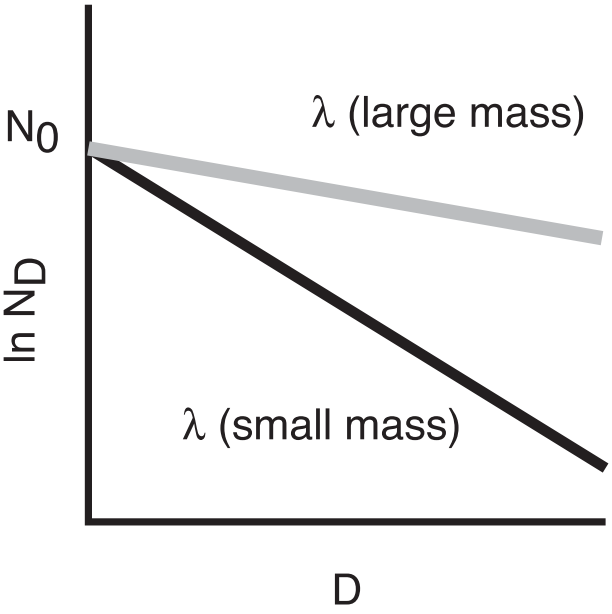

FIG. 11-1. Exponential (Marshall–Palmer) particle size distribution for number of particles (N_D) vs diameter (D), which assumes a fixed intercept N_0 with slope λ determined by particle mass content.

[4] Tripoli and Cotton (1980) is an example of the fixed λ approach.

Whatever assumptions are made, bulk MPs employ integrations of the continuous collection equation (CCE) over the presumed PSDs to handle processes such as the accretion of cloud droplets by more swiftly falling raindrops. The CCE is based on the idea that a particle sweeps out a cylindrical volume as it falls relative to still air and/or other particles (Kessler 1969; Lin et al. 1983). Kessler (1969) further approximated the CCE for this process and also handled the creation of new raindrops from cloud droplet aggregation (the autoconversion process) in a particularly simple way. Along with a saturation adjustment for transferring mass between vapor and cloud water, and an equation for rainwater evaporation (cloud droplets were assumed to evaporate instantly in subsaturated air), the Kessler scheme can be implemented in just a few lines of code.

By contrast, schemes that incorporate various species of ice (such as free-floating ice crystals, low-density snow, medium-density graupel, and/or high-density hail), more sophisticated PSDs and/or higher moments are much, much more complicated, and can claim a sizable fraction of the computing time required for a given simulation. These ''ice-bearing schemes'' embody many additional assumptions (including collision efficiencies for various two- and three-body collisions, ice multiplication, riming, melting, etc.) and require considerably more computational effort. Numerous MPs exist, which often differ solely with respect to ostensibly subtle factors such as the fall speed of graupel particles or how efficiently ice crystals evolve into snow. As discussed in section 4, research has shown these factors can have an outsized effect on TC structure, motion, and intensity.

b. *Radiation and interaction with hydrometeors*

Atmospheric gases such as water vapor, carbon dioxide, and ozone are selective absorbers of thermal radiation. These gases, other particles, and Earth's surface also scatter and emit radiation, nearly all of the latter occurring in the LW portion of the radiation spectrum. As radiative processes represent an important part of the energy balance of the atmosphere and Earth's surface, operational simulations of TCs typically make use of a radiation parameterization, of which several are available in the WRF platform (including RRTM, RRTMG, CAM, Goddard, Dudhia, Fu–Liou–Gu, and GFDL). These codes represent attempts to model very complex and time-consuming processes in a more efficient manner, but can still be quite computationally expensive.

When a multiday simulation is initialized with the Jordan (1958) sounding in which convection is not permitted (see P7), these radiation schemes tend to produce

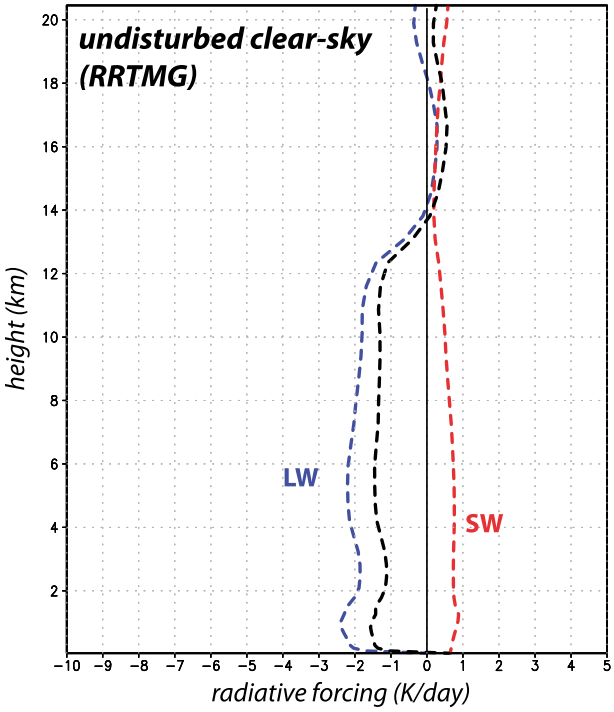

FIG. 11-2. Tendencies (K day^{-1}) averaged over space and through one diurnal cycle for LW (blue), SW (red), and net (black) radiation from an HWRF simulation undisturbed by convection using the RRTMG parameterization. From P7.

about 1 K day^{-1} of SW warming and about 2 K day^{-1} LW cooling in the lower-to-middle troposphere, for a net radiative forcing of about -1 K day^{-1} averaged through the diurnal cycle (Fig. 11-2). These profiles appear reasonable for a moist environment [cf. Figs. 3.18 and 4.15a in Liou (2002)] and variability among available schemes appears minor (not shown). By contrast, many idealized studies either neglect diabatic forcings associated with radiation or handle it in a very simple manner. As an example, Rotunno and Emanuel (1987) used Newtonian cooling for the express purpose of preventing the model atmosphere from straying too far from the initial hurricane environment.

The above describes background or ''clear-sky'' radiation, as it is independent of condensate content and convective activity. Hydrometeors also participate in the absorption of SW, and absorption and emission of LW radiation, representing the CRF. The various parameterizations handle resolved condensate, as well as subgrid-scale clouds, in different ways. Stephens (1978) related CRF to the cloud water path, which is the integral of cloud water content over depth. This concept was implemented in the original RRTM LW and Dudhia SW schemes via specified, species-dependent absorption and emission coefficients (ϵ). For LW (Table 11-2),

TABLE 11-2. LW absorption/emission coefficients (ϵ) used in the original RRTM scheme.

Species	Coefficient ($m^2\,g^{-1}$)	Relative magnitude to cloud droplets for 1 kg m^{-3} mass content
Cloud droplets q_c	0.144	—
Cloud ice q_i	0.0735	0.510
Snow q_s	0.00234	0.016
Rain drops q_r	0.00033	0.002
Graupel q_g	0.0	0.0

the coefficient assigned to free-floating cloud ice (ϵ_i) is one-half that used for liquid droplets, but is over 31 times that for snow (ϵ_s) and about 222 times the absorption coefficient applied for rainwater (for mass contents of 1 kg m^{-3}). In the RRTM LW scheme, graupel is completely ignored. In the P3 study, ϵ_i and ϵ_s were varied to crudely illustrate the effect of shifting condensate mass among various species, which in some cases had a nontrivial impact on TC track. RRTMG has introduced new ways of handling hydrometeor effects, which produce qualitatively similar results but are less straightforward to adjust.

4. Synopsis of CRF impacts

a. Microphysics influences on TCs

For some time, we have appreciated that cloud microphysical assumptions can materially influence TC intensity, but with considerable variability among the real and idealized cases examined, which suggests that microphysical processes are both important and an integral part of forecast uncertainty [e.g., see review by Tao et al. (2011)]. For example, Lord et al. (1984) concluded that including ice processes resulted in a significantly stronger storm, and McFarquhar et al. (2006) found intensity generally increased as graupel fall speeds were increased. In contrast, P2 found that faster tangential winds were simulated when graupel formation was suppressed in the Purdue–Lin (Lin et al. 1983; Chen and Sun 2002) ice MP scheme. Excluding graupel increased the storm intensity by about 10% relative to the original version of Purdue–Lin, which made it about 30% stronger than its warm rain (Kessler) counterpart (see P2's Fig. 14). In other studies, excluding ice produced TCs that intensified more rapidly and/or attained higher intensity at maturity (e.g., Hausman et al. 2006; Li and Pu 2008; Stern and Nolan 2012).

Thus, microphysical parameterizations may incorporate a variety of processes that individually may increase or suppress TC organization and/or intensity; however, the net result is sensitively dependent on precisely how the various processes combine. Many of these processes involve diabatic heating or cooling. Wang (2002) and Zhu and Zhang (2006) showed that excluding some sources of diabatic cooling encouraged more rapid intensification and lower central pressures during TC maturity. In particular, Wang's (2002) simulation called NMLT (for "no melting"), which neglected all melting of snow and graupel as well as rain evaporation, became organized much more rapidly and reached a substantially lower sea level pressure (SLP) than the other simulations (Fig. 11-3). Bu (2012) studied the organization of TCs in an axisymmetric version of the CM1 model, primarily using versions of the Kessler MP. She found that TC organization was most rapid and efficient when condensation was immediately removed upon creation, which excludes both diabatic cooling from evaporation and hydrometeor loading, but that simply preventing rainwater formation alone was not sufficient (Fig. 11-4) to hasten storm organization.

Prior studies have shown that TC behavior (e.g., Willoughby et al. 1984) and structure (e.g., P1–P7) are both sensitive to microphysics. The symmetric components of the 10-m wind speed from the 13 simulations conducted for the P3 study (Fig. 11-5) were obtained by

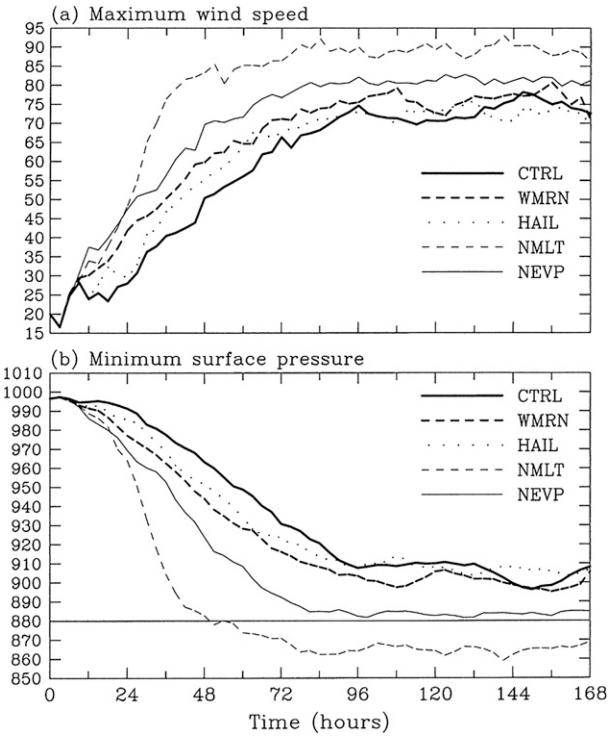

FIG. 11-3. Evolution of (a) maximum wind speed (m s^{-1}) at the lowest model level and (b) minimum SLP (hPa) for several experiments, including the control run (CTRL), a warm rain without ice (WMRN), a simulation including hail (HAIL), and runs in which melting (NMLT) or evaporation (NEVP) were neglected. From Wang (2002).

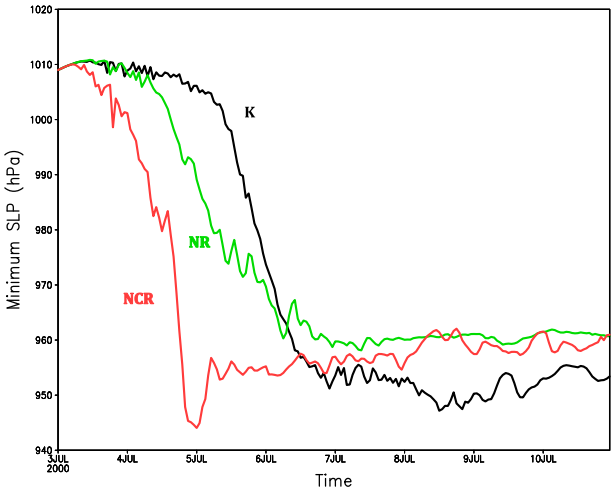

FIG. 11-4. Minimum SLP from axisymmetric CM1 model simulations made using microphysical variants of the warm rain Kessler (K) scheme. Simulations NR and NCR prevented the formation of raindrops and both cloud droplets and raindrops, respectively. From Bu (2012).

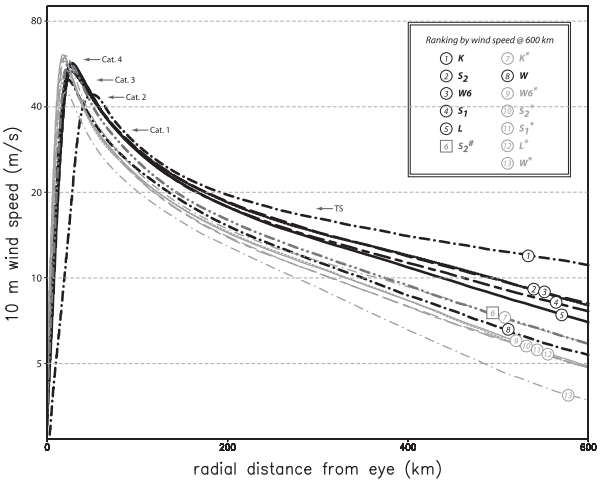

FIG. 11-5. Symmetric components of the 10-m wind speed ($m\,s^{-1}$), temporally averaged over a diurnal cycle in a vortex-following fashion, from ARW simulations conducted for the P3 study. Microphysical schemes considered include Kessler (K), two versions of Seifert–Beheng (S_1 and S_2), WSM3 (W), WSM6 (W6), and Purdue–Lin (L); see Table 11-3. Asterisks indicate CRF-off runs and $S_2^{\#}$ is the LW absorption sensitivity test from P3. Note the vertical axis is log scaled.

temporally averaging the field in a vortex-following fashion over the final day of a 4-day simulation, and then averaging again in the azimuthal direction; see P2 for more information. In addition to the warm rain Kessler (K) scheme, five ice-bearing schemes were considered: the single-moment WRF single moment three-class [WSM3 (W)] and six-class [WSM6 (W6)] and Purdue–Lin (L) MPs, as well as two versions of the Seifert and Beheng (2006) double-moment parameterization (S_1 and S_2) that differ with respect to ice-to-snow conversion (Table 11-3). Note that the warm rain scheme results in a storm with a uniquely wide eye and broad outer wind profile compared to the structure simulated with the ice-bearing schemes; this will be explored in more detail presently.

Even fairly subtle variations in outer wind strength are potentially very important as these winds influence TC motion owing to the "beta drift." Differential advection of planetary vorticity by the storm's cyclonic circulation creates gyres that combine to establish a "ventilation flow" across the vortex (e.g., Holland 1983; Fiorino and Elsberry 1989) that impels motion on a curved Earth, even in environments with no mean current. Using a barotropic model, Fiorino and Elsberry (1989) demonstrated that this ventilation flow influences the speed and direction of TC motion (Fig. 11-6). Even though the wind profiles (Fig. 11-6a) only varied beyond radius r = 300 km from the center, distinctly different tracks (Fig. 11-6b) are predicted in the experiment, with the strongest outer winds resulting in both the most rapid and most relatively westerly motion.

A straightforward application of Fiorino and Elsberry's (1989) findings to the Fig. 11-5 profiles would predict that the relatively strong outer winds of the Kessler TC would lead to the fastest motion and the most northwestward track, while the simulated storms with weaker cyclonic flow at large radii would be expected to have slower and more northward motions. This is indeed what occurred in P3's experiment (Fig. 11-7a).[5] After an organizational stage, the warm rain storm moved northwest at over 9.7 km h^{-1} (2.7 m s^{-1}), while the other storm motions were much slower with direction during maturity that varied more than speed (4–6 km h^{-1}, 1–1.7 m s^{-1}). Such motions fall into the range of typical beta drift speeds of 1–4 m s^{-1} (cf. Holland 1983; Chan and Williams 1987). Figure 11-8 depicts motion during the last 12 h of the integration for a version of P3's experiment, augmented to include the Thompson and Ferrier (Thompson et al. 2008; Ferrier et al. 2002) MPs and additional radiative schemes (Table 11-1). The variation in motion directions implies a widening range of tracks with time.

In a warm-core vortex, the poleward-directed ventilation flow established by the beta gyres should weaken with height (e.g., Bender 1997), which then results in a northwesterly to northerly vertical shear across the TC that acts to enhance inner-core convective activity on its

[5] Keep in mind the model has no land, and a coastline was provided for scale only.

TABLE 11-3. Microphysics schemes referenced in this paper.

Symbol	Name	Reference(s)
K	Kessler (warm rain)	Kessler (1969)
L	Purdue–Lin	Lin et al. (1983), Chen and Sun (2002)
W	WSM3 (WRF single moment, 3-class)	Hong et al. (2004)
W6	WSM6 (WRF single moment, 6-class)	Hong et al. (2004), Dudhia et al. (2008)
T	Thompson	Thompson et al. (2008)
F	Ferrier	Ferrier et al. (2002)
S_1, S_2	Seifert–Beheng	Seifert and Beheng (2006), Fovell et al. (2010b)

downshear and downshear-left flanks (e.g., Frank and Ritchie 1999; Corbosiero and Molinari 2002). Consistent with this interpretation, a sample of cases using P5's experimental design reveals lower tropospheric average vertical motions that are generally concentrated on the storm's eastern and southeastern sides (Fig. 11-9), although notice that the patterns and degrees of asymmetry vary among the MP schemes. Note that the simulation with the warm rain MP generated the widest and most symmetric updraft pattern, which is consistent with its especially broad wind profile (Fig. 11-5).

This asymmetric diabatic heating also appears to modulate TC motion in ways that compete or cooperate with the ventilation flow, depending on the orientation of the asymmetry pattern that varies depending on microphysical assumptions. Wu and Wang (2000) employed a potential vorticity (PV) diagnostic for TC motion in which the relative contributions to the PV tendency (PVT) due to the advection (horizontal and vertical, herein labeled HA and VA), friction, and a term proportional to gradients of diabatic heating, Q (herein labeled DH). Specifically, the wavenumber-1 components of the PVT contributions were computed, using a least squares technique (see Wu and Wang 2000). The combination of the DH, VA, and the (typically small) residual terms will be called DH*. Since the contributions of all terms tended to shift with height (Fig. 11-10), however, they are not truly independent and strongly modulate each other (cf. P5). Papers P3 and P6 addressed the height variation by averaging the terms vertically through the lower troposphere above the boundary layer; P6 noted that the lack of independence encourages a fundamentally qualitative and comparative application.

The arrows on Fig. 11-9 represent storm motion (C) and the contributions to PVT from DH and DH*. Although not shown, the horizontal advection term can be inferred as the difference between C and DH*; as expected, HA is generally directed northwestward, since it is in large part the advection of PV by the ventilation flow. Since the Kessler TC (Fig. 11-9a) has the most symmetric vortex, the magnitude of DH is very small and DH* is effectively zero, so the diabatic forcing in this simulated TC is not effective at opposing the motion due to the ventilation flow, which is substantial owing to the strength of this TC's outer wind profile.

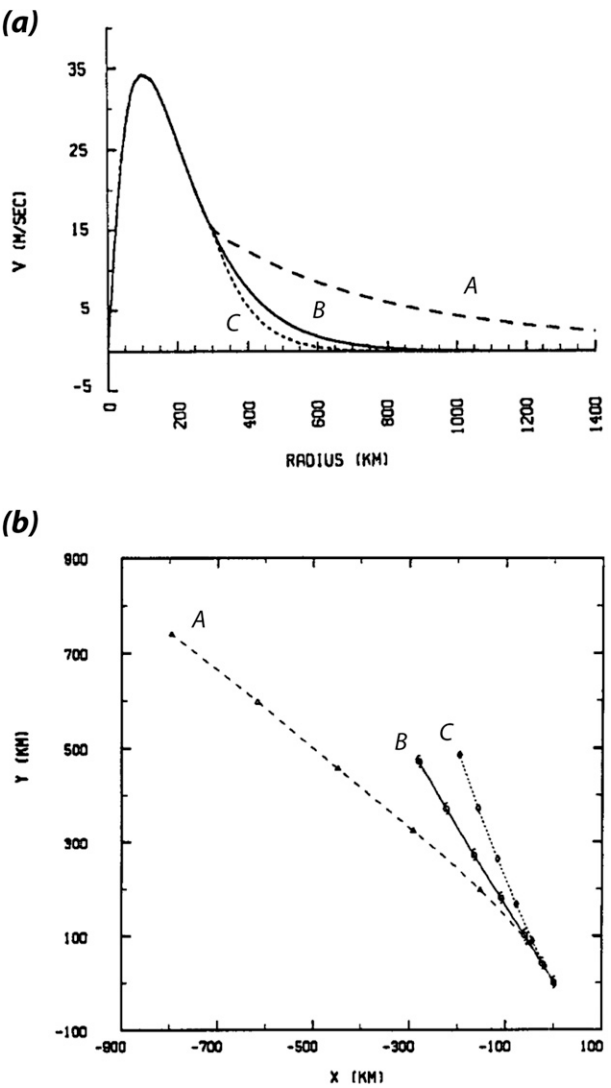

FIG. 11-6. (a) Initial tangential wind profiles and (b) corresponding tracks to 72 h from the Fiorino and Elsberry (1989) experiment. In (b), markers are separated by 12 h.

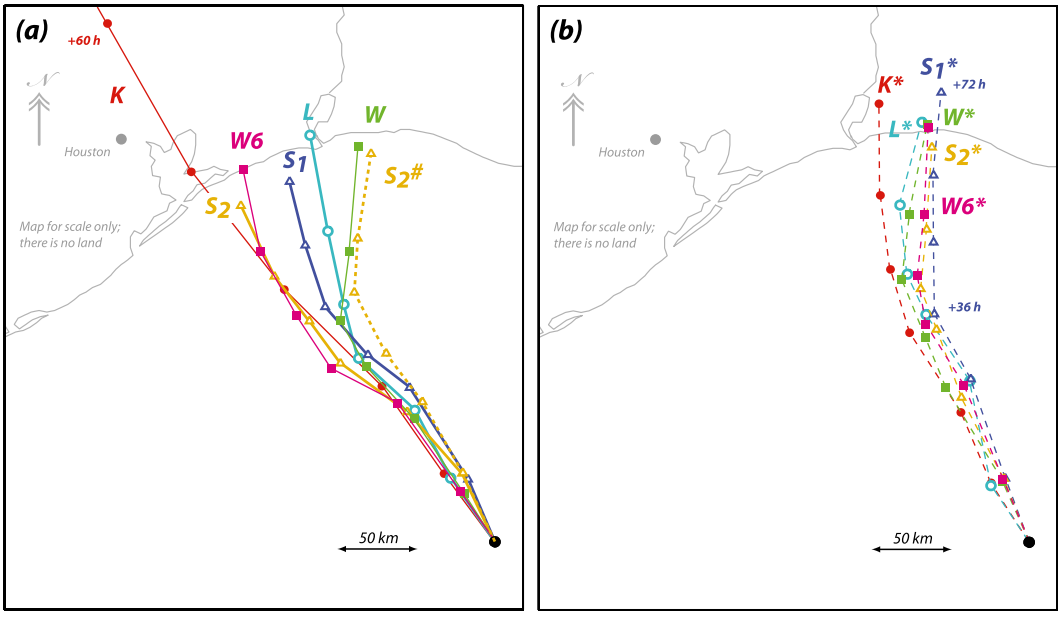

FIG. 11-7. 12-hourly cyclone positions over 72 h for simulations K, L, W, W6, and S_1 and S_2 (see Fig. 11-5 and Table 11-3) with CRF (a) on and (b) off. The 72-h K simulation position is beyond the subdomain depicted. The U.S. Gulf Coast segment is included only for scale as the model has no land. Simulations employed WRF v. 2.2.1, RRTM LW, and Dudhia SW. Adapted from P3.

Consequently, the Kessler TC has the fastest motion among the bubble-initialized storms.

In contrast, the simulations with ice-bearing MPs all have weaker outer wind profiles (Fig. 11-5) as well as substantially more asymmetric vertical velocity and heating patterns (Fig. 11-9). The S_2 (with RRTM/Dudhia), T@ (Thompson, with RRTMG), and F (Ferrier, with GFDL radiation) cases (Figs. 11-9b–d) are examples of the range of TC structures and translations among these storms. Among them, the T@ case has the fastest translation speed and moved north-northwestward at 5.9 km h^{-1} (1.6 m s^{-1}), which is substantially slower than the K storm but still exceeds the motions of S_2 (3.6 km h^{-1} or 1 m s^{-1}) and F/GFDL (3.8 km h^{-1} or 1.1 m s^{-1}). The somewhat faster storm motion in the T@ simulation may have been due to the small contribution of the diabatic heating term in the direction of beta drift (Fig. 11-9b), even though the storm has weaker outer winds relative to the K case.[6] In the S_2 simulation (Fig. 11-9c), the diabatic heating term appears to be opposing the beta drift, while the concentrated asymmetric heating on the F/GFDL storm's eastern flank (Fig. 11-9d) may explain why it developed the most eastward track (Fig. 11-8). Naturally, this particular aspect of storm motion could not be captured in Fiorino and Elsberry's

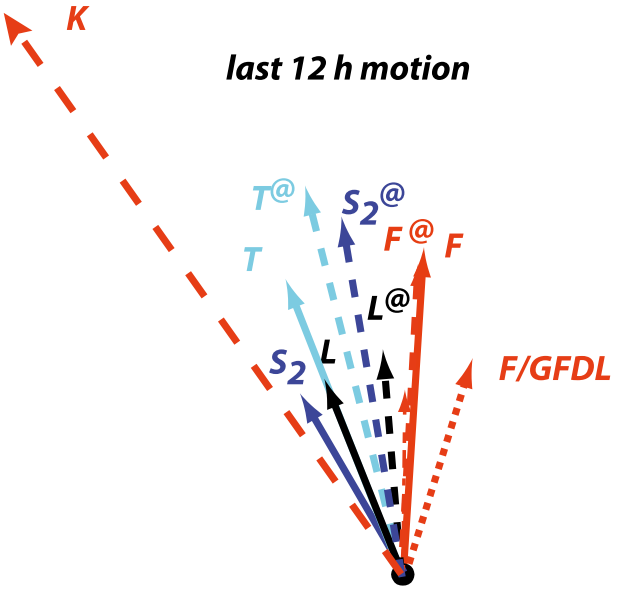

FIG. 11-8. Storm motion vectors for the 60–72-h period from simulations made for the P3 study (see Fig. 11-7 caption). The augmented P3 study adds simulations using WRF v. 3.2 employing Thompson (T) and Ferrier (F) microphysics, the RRTMG LW and SW (indicated by @ sign) schemes, and GFDL radiation. Adapted from P3.

[6] It needs to be kept in mind that while microphysical diabatic heating, Q, logically tends to be well correlated with vertical velocity, the DH term actually consists of the gradients of Q multiplied by vorticity, along with other terms. This is why the DH vectors may not point toward where the air is ascending most strongly. See P6 for more information.

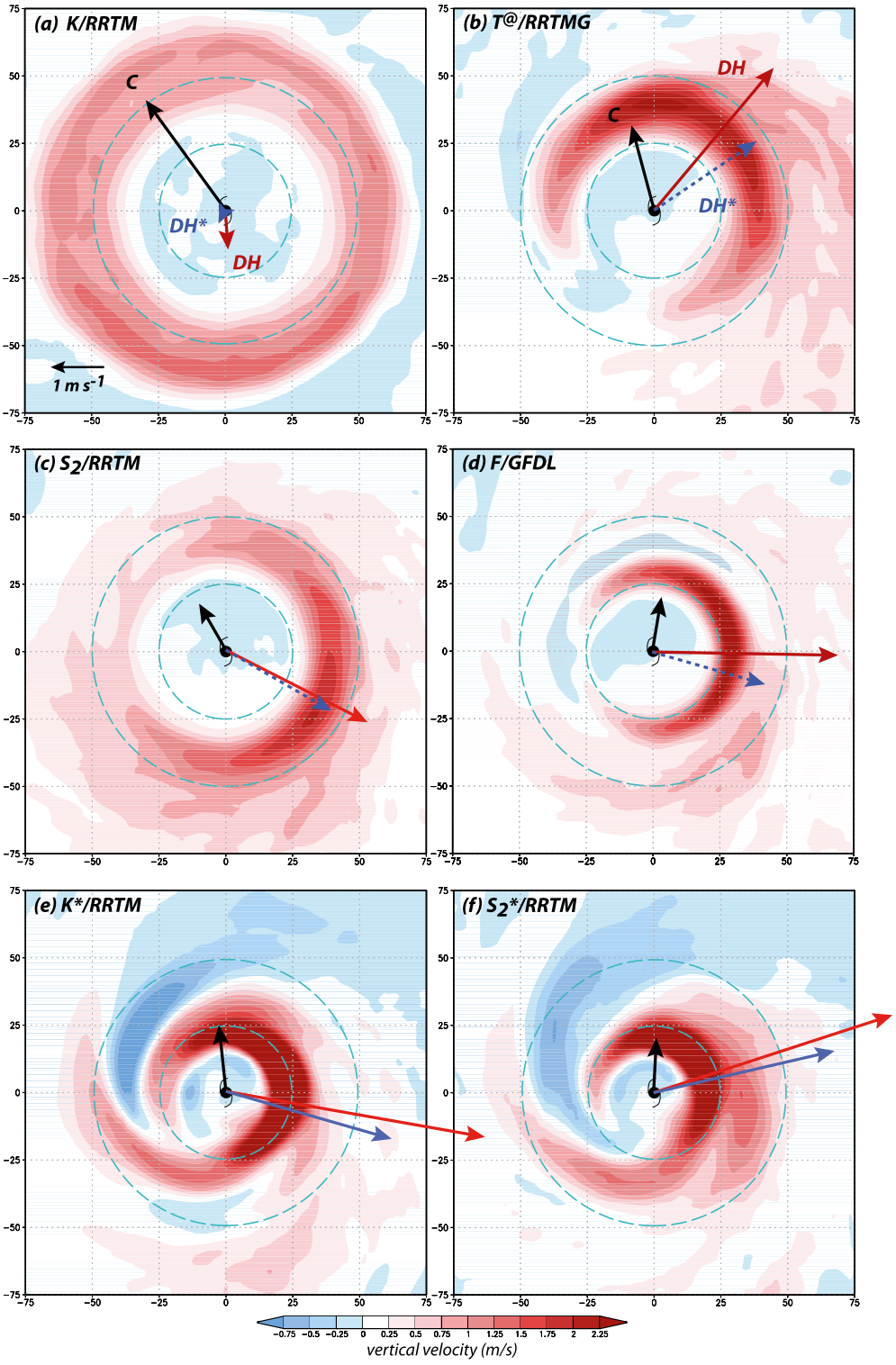

FIG. 11-9. Vertical velocity averaged from the surface to 500 hPa (mass-weighted) and over 150 km ×150 km portions of the model's single, 4-km resolution domain, from P3 and augmented P3 simulations (Table 11-1) using various MP and radiation schemes. Fields were averaged in a vortex-following manner over day 4 of the simulations. Superposed are vectors indicating storm motion (C) and contributions to motion from diabatic heating (DH) and a combination of DH and vertical advection (called DH*). The top of the figure represents north.

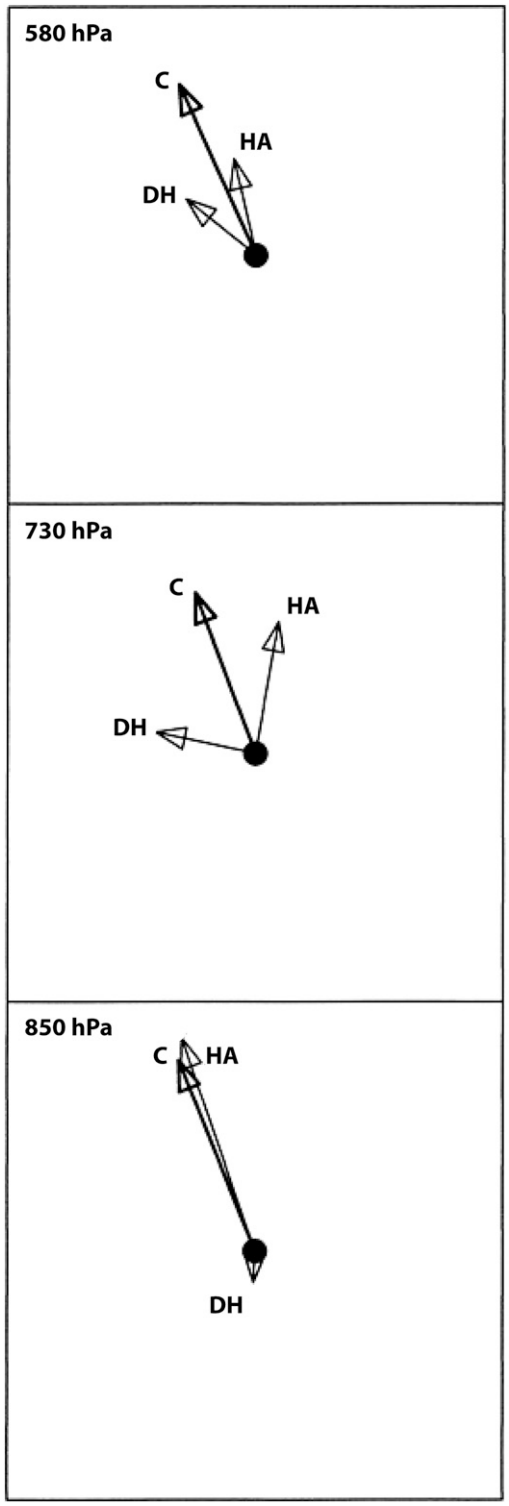

FIG. 11-10. Contributions of horizontal advection (HA), vertical advection (VA), and diabatic heating (DH) to storm translation (*C*) at 36 h at three levels from one of Wu and Wang's (2000) experiments. Maximum vector length is 2.9 m s^{-1}. Adapted from Wu and Wang (2000).

(1989) barotropic model, but it appears to make an important, and possibly crucial, contribution to the storm motion.

Sensitivity to microphysics has been most pronounced in our experiments using the bubble initialization. In P5's study, simulations commencing with artificially supplied initial outer wind profiles defined by a structural parameter, α (see section 4c), appeared to be quite "resilient" to the effects of the beta shear, and thus less likely than their bubble counterparts to develop asymmetric updraft (Fig. 11-11) and heating structures. As a consequence, these simulated TCs had significantly faster translation speeds than might have been expected from their symmetric outer wind profiles (Fig. 11-13). For example, note that the $\alpha = 0.75$ run had outer winds comparable to the bubble TC, but had a 2.6 times faster translation speed (2.43 vs 0.92 m s^{-2}; see P5's Table 2). The realism of the resilient bogussed vortices awaits closer examination.

PVT analysis was employed in P6 to examine how and why TCs tend to change direction and speed as they approach a mountainous island such as Taiwan, which contains a prominent central mountain range (CMR) roughly parallel to its east coast, by introducing an obstacle resembling Taiwan into the aquaplanet framework (Fig. 11-13). A novel element of the P6 study was that the Taiwan-like island was made of water, which removes potential complications such as changes in surface friction and fluxes after landfall. The bogus-initialized TC initially had little asymmetry in its heating and rainfall fields (reflecting vortex resilience) as it approached the obstacle island from the southeast. With the weak basic current included in this experiment, the TC had a relatively rapid translation during this period (Figs. 11-13a,b). Once the cyclonic storm circulation began being affected by the CMR, however, the TC direction and speed changed in a manner consistent with the influence of the DH* term (Figs. 11-13c,d). Speed and direction variations continued as the TC crossed the CMR, which affected the orientation of the topographically driven diabatic forcing (Figs. 11-13e,f). In summary, this study clearly reveals that terrain-induced asymmetries in diabatic heating suffice to profoundly impact the motion of a cyclonic vortex over an island barrier.

b. Cloud-radiative forcing

We have seen that microphysics clearly exerts an important influence on TC track and structure. The P3 experiment, however, revealed a surprising finding: these variations in track and structure largely disappeared when the radiative forcing owing to clouds was neglected, rendering clouds essentially transparent to radiation. The first indication that radiation was important came in P2, which showed that while the

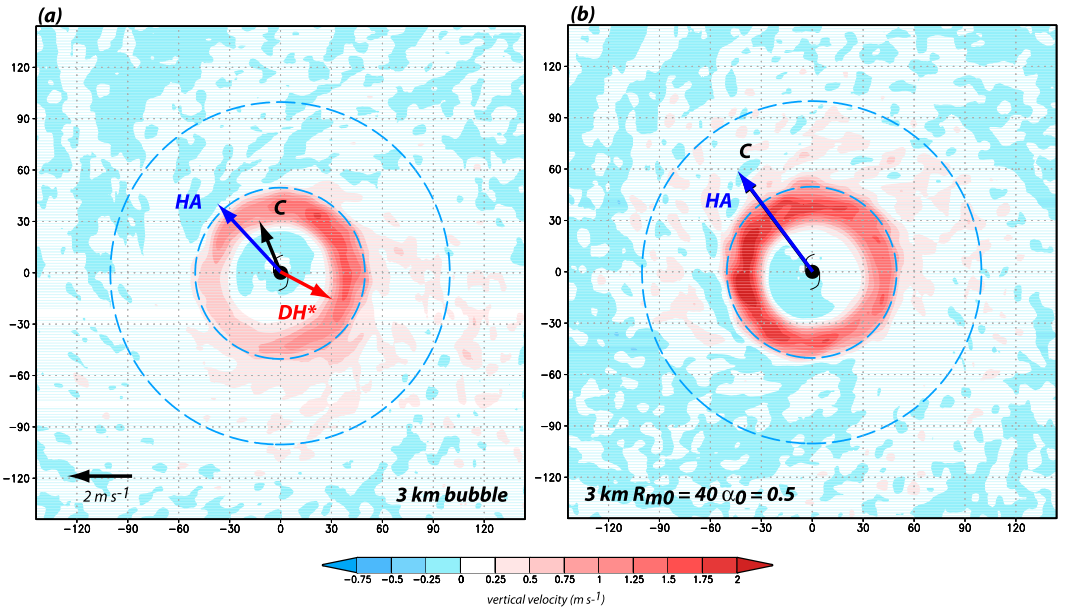

FIG. 11-11. Mass-weighted vertically averaged vertical velocity over the lowest 4.3 km (shaded) for the last day of 4-day simulations using (a) the bubble initialization and (b) a bogus vortex, from P5's high-resolution simulations (see Table 11-1); R_{m0} and α_0 are initial values used in the Rankine formula [(11-3)]. As in Fig. 11-9, vectors represent storm motion (C) and the HA and DH* motion contributions. For (b), the DH* term is essentially zero. Adapted from P5.

K storm's track was not sensitive to which radiation parameterization (RRTM or CAM) was selected, storm translation was dramatically slower when no radiative scheme was used (P2's Fig. 9). That was a crude version of P3's and P7's experiments in which only the specific influence of hydrometeors on radiation was deactivated, but the background (clear-sky) LW and SW forcings were retained. Figure 11-7b reveals the members of P3's microphysical ensemble had a similar speed and direction of motion evolution, including especially the Kessler version K*, which is clearly the most dissimilar from its ''cloudy'' counterpart.[7]

The shift to slower, more northward motions is consistent with the storms' weaker symmetric outer wind profiles (Fig. 11-5). Note further that deactivating CRF materially altered the storm structure (Figs. 11-9e,f; see also P3's Figs. 2e–h). The CRF-off cases tend to be narrower, even more asymmetric, and resemble each other far more than they do any of the CRF-on cases.[8] The shift with the warm rain MP (Figs. 11-9a,e) is especially dramatic, and the similarity between K* and S_2^* is striking, especially with respect to the relatively strong and deep downdrafts that appear in the northwestern quadrants of these storms that are absent when CRF is active. Note that the F/GFDL case (Fig. 11-9d) has intermediate characteristics between the CRF-on and CRF-off cases. P7 showed that this model physics

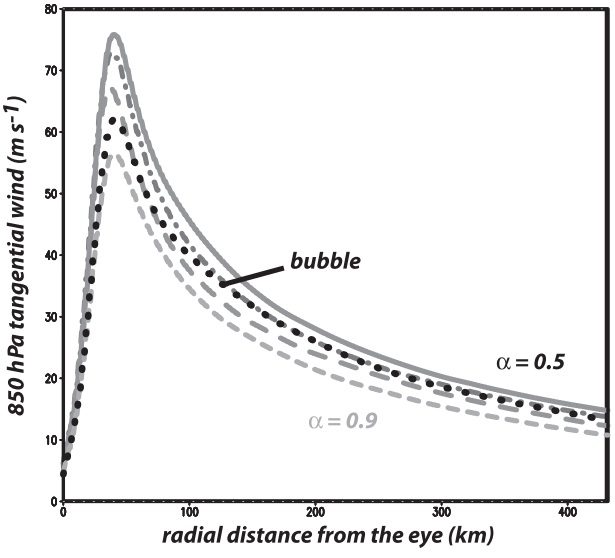

FIG. 11-12. Symmetric components of 850-hPa wind speed ($m\,s^{-1}$) for 3-km resolution experiments constructed from vortex-following composites averaged during the final 24-h period. The α and bubble designations refer to the initializations, and α values shown are 0.5 (solid), 0.625 (dashed-dotted), 0.75 (long dashed), and 0.9 (short dashed). Adapted from P5.

[7] Deactivation of cloud-radiative forcing is indicated with an asterisk (e.g., K*, S_2^*, etc.).

[8] As noted earlier, the intensity tendency noted in P3 is contradicted in other experiments, which is why it is not emphasized here.

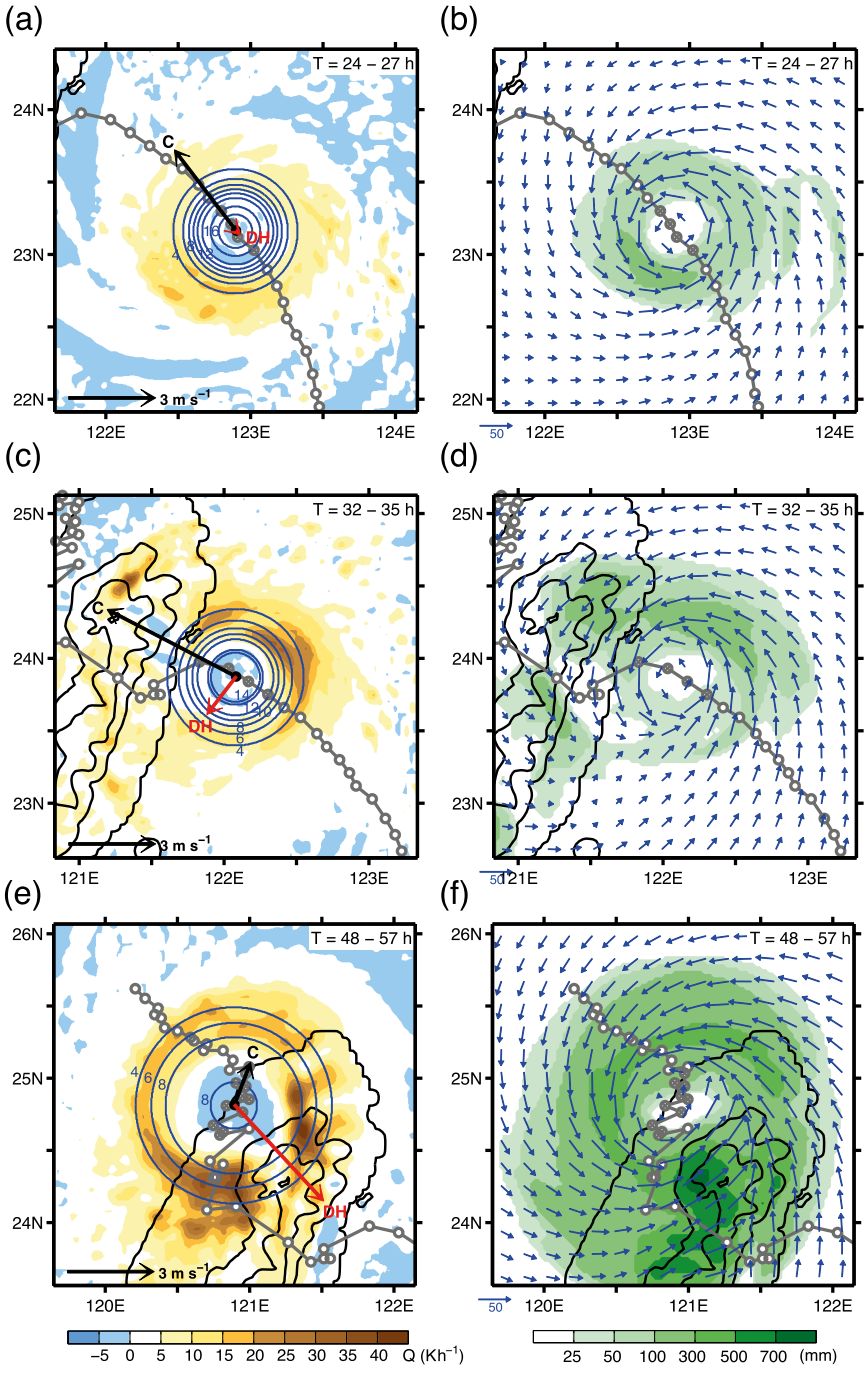

FIG. 11-13. Vortex-following composite fields averaged over three periods (T) from one of P6's experiments. (left) Vertically averaged diabatic heating Q (color shaded, K s^{-1}) and symmetric PV structure [blue contours, unit is PVU (1 PVU = 10^{-6} m^2 s^{-1} K kg^{-1})], along with motion C (black), and DH (red) terms. (right) Composite rainfall (shaded) and wind vectors at the lowest model level. Averaging periods are (a),(b) 24–27, (c),(d) 32–35, and (e),(f) 48–57 h, and indicated by filled circles on the superposed storm tracks. From P6.

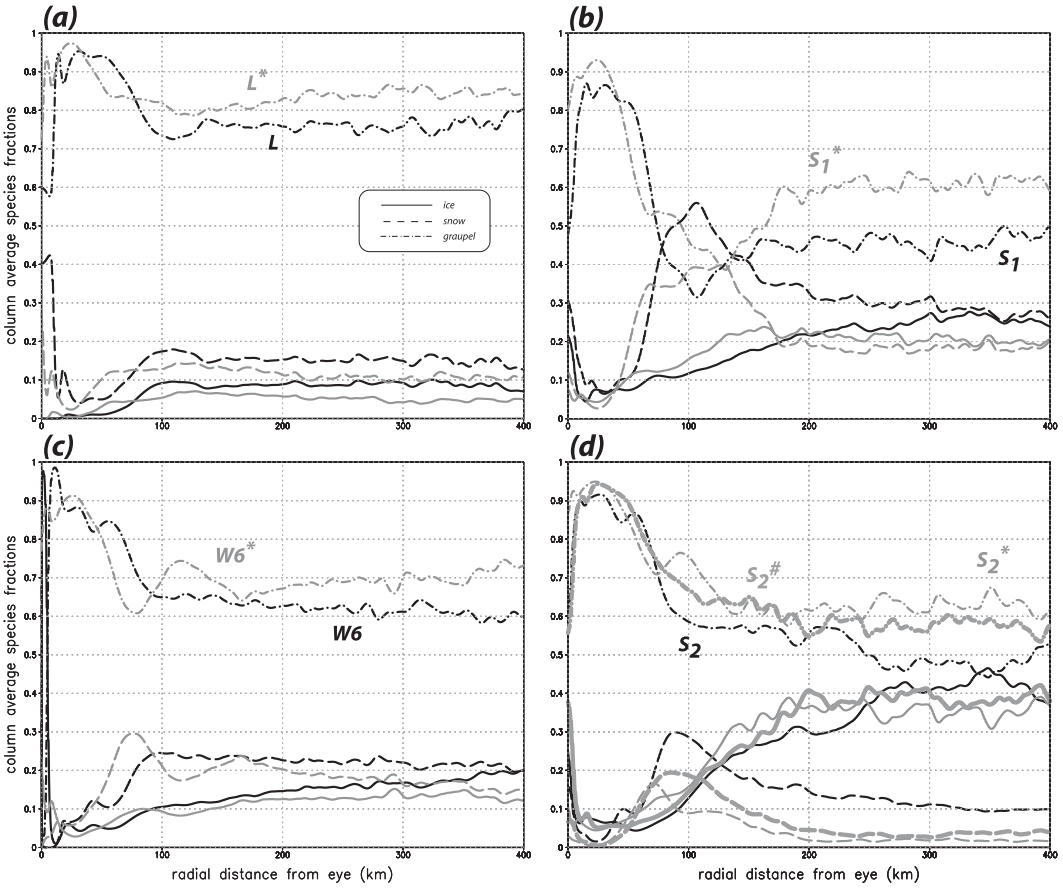

FIG. 11-14. Ice species fractions vs radial distance from the eye computed using symmetric components from temporally averaged vortex-following composites for simulations using versions of the (a) L, (b) S_1, (c) W6, and (d) S_2 MPs (see Table 11-3). Asterisks denote CRF is ignored; simulation $S_2^{\#}$ treats cloud ice as snow for radiative calculations. Augmented from P4.

combination, which closely resembles that employed in the operational HWRF, results in a substantially reduced cloud-radiative forcing owing to how that parameterization is implemented (see P7 for more information).

As indicated in section 3a, MP schemes may range from the simple to complex with respect to how many hydrometeor species are included and precisely how they are handled. However, it seems very clear that the major reason why microphysics can influence TC structure and motion is because condensate particles can influence radiative heating and cooling. CRF sensitivity therefore emerges precisely because MPs tend to produce different amounts of condensate species (Fig. 11-14) that have significantly disparate radiative impacts when CRF is active. A scheme that produces much more cloud ice than snow, such as S_2 (Fig. 11-14d), should have much larger CRF than ones with a swift evolutionary path to graupel such as the L (Fig. 11-14a) or W6 (Fig. 11-14b) MPs. Note that over 70% of the azimuthally and column-averaged ice mass in the L storm is in the form of graupel (Fig. 11-14a), which observations (McFarquhar and Black 2004; McFarquhar et al. 2006) suggest is unreasonably large, and less than 10% is in cloud ice. Of course, the warm rain scheme generates copious amounts of cloud droplets, which are presumed to be more radiatively active than even cloud ice (not shown), which is why rendering them transparent to radiation had such a profound effect on the storm. It is probably easier to identify unrealistic condensate combinations than realistic ones, but these examples demonstrate that the consequences of these arguable microphysical assumptions are not small.

P3 further explored sensitivity to LW radiation via manipulation of the RRTM scheme's absorption coefficients for MP schemes S_2 and W6 by making snow either completely transparent to radiation (simulations $S_2\hat{}$ and W6$\hat{}$) or by treating cloud ice similarly to less radiatively active snow (simulations $S_2^{\#}$ and W6$^{\#}$). Rendering frozen condensate progressively more transparent resulted in eastward shifts of the simulated tracks

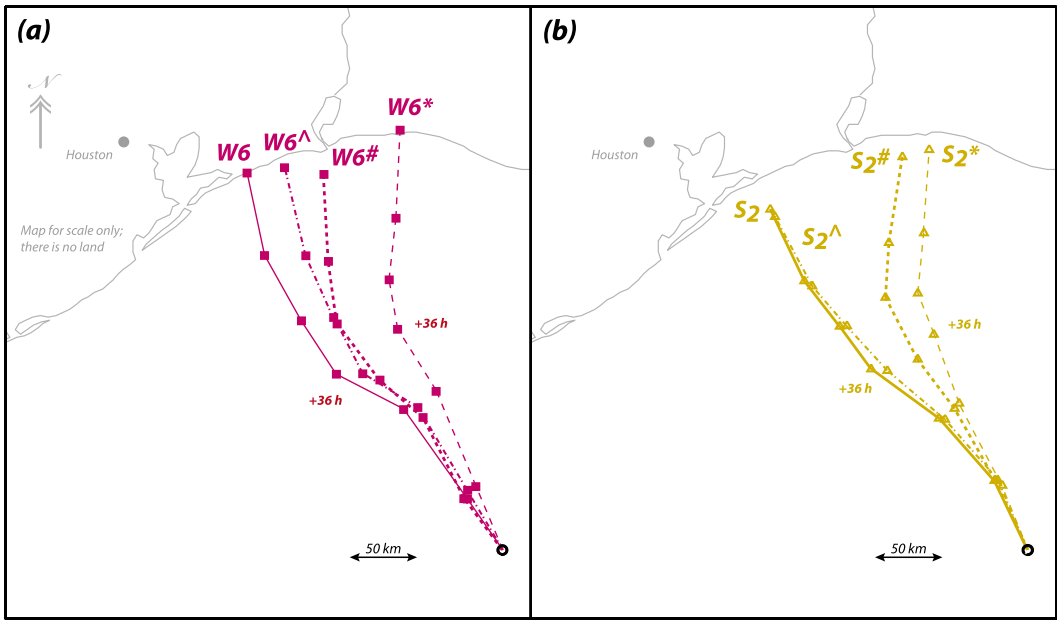

FIG. 11-15. As in Fig. 11-7, except for versions of W6 and S_2 that demonstrate LW absorption/emission coefficient sensitivity. Simulations designated with the hash symbol (#) treat cloud ice as snow for LW calculations, while those designated with the caret (^) ignore the contribution of snow. Adapted from P3.

(Fig. 11-15) as the magnitude of the storm outer winds decreased (Fig. 11-5), even though the relative distribution of frozen hydrometeors among the ice species was little affected (Figs. 11-14c,d). Among these three S_2 variants, we see that $S_2^{\#}$ falls between the other two with respect to the radial extent of its microphysical diabatic heating and tangential wind fields (Figs. 11-16a–c). Although the association between the $1\,\mathrm{K\,h^{-1}}$ diabatic forcing and $20\,\mathrm{m\,s^{-1}}$ wind contours with respect to position in these figures is very likely coincidental, it is clear that both extend radially farther outward as the radiative footprint of ice increases. These fields can be compared to the P7 study that used HWRF and Thompson microphysics (see their Figs. 4, 5, and 8).

The net cloud-radiative forcing from the combination of LW and SW averaged through the diurnal cycle consists of cooling along the top of the cloud anvil and warming within the cloudy region (Fig. 11-16d–f; see also P7's Figs. 5 and 6). This pattern depends on CRF (and thus is absent in S_2^{*}; Fig. 11-16e) and is far better developed when LW absorption and emission by ice is enhanced. Vertical profiles of temporally and spatially averaged net radiation (Fig. 11-17; see also P7's Fig. 7) reveal that only the CRF-on case possessed net warming in the troposphere within 350 km of the storm center.[9] P7 demonstrated that the sign reversal for net radiation relative to clear-sky conditions in the CRF-active case was nearly all due to the hydrometeor effect on longwave absorption as SW radiation failed to penetrate the thick ice cloud (P7's Fig. 6). The CRF field is considerably more extensive radially for the CRF-active case (Fig. 11-16d), which reflects an expanded anvil (contoured field) in that case.

The S_2 variants examined herein represent the range of structural variations produced by other MP schemes in our experiment since altering the LW hydrometeor coefficients essentially mimics shifts in frozen water speciation. There is also some sensitivity to the radiation parameterization, especially with respect to the LW cooling at the cloud top. For example, employing RRTMG for LW and SW (in place of RRTM and Dudhia) with the S_2 scheme reduces the net radiative forcing by about one-half (simulation labeled $S_2^{@}$ in Fig. 11-17), which is a consequence of both reduced LW cooling and increased SW absorption (not shown). However, net radiative forcing is little affected at lower levels, and the role of cloud-top cooling in TC structure appears to be quite limited anyway (see next subsection).

c. *How and why CRF influences TC structure*

After documenting comparable differences between CRF-active and CRF-inactive TCs simulated using a semi-idealized version of the three-dimensional HWRF with Thompson MP and RRTMG radiation, P7 offered an explanation for how and why radiative forcing associated with hydrometeors causes radially expanded wind

[9] The clear-sky profiles shown for comparison were obtained in the manner described in P7.

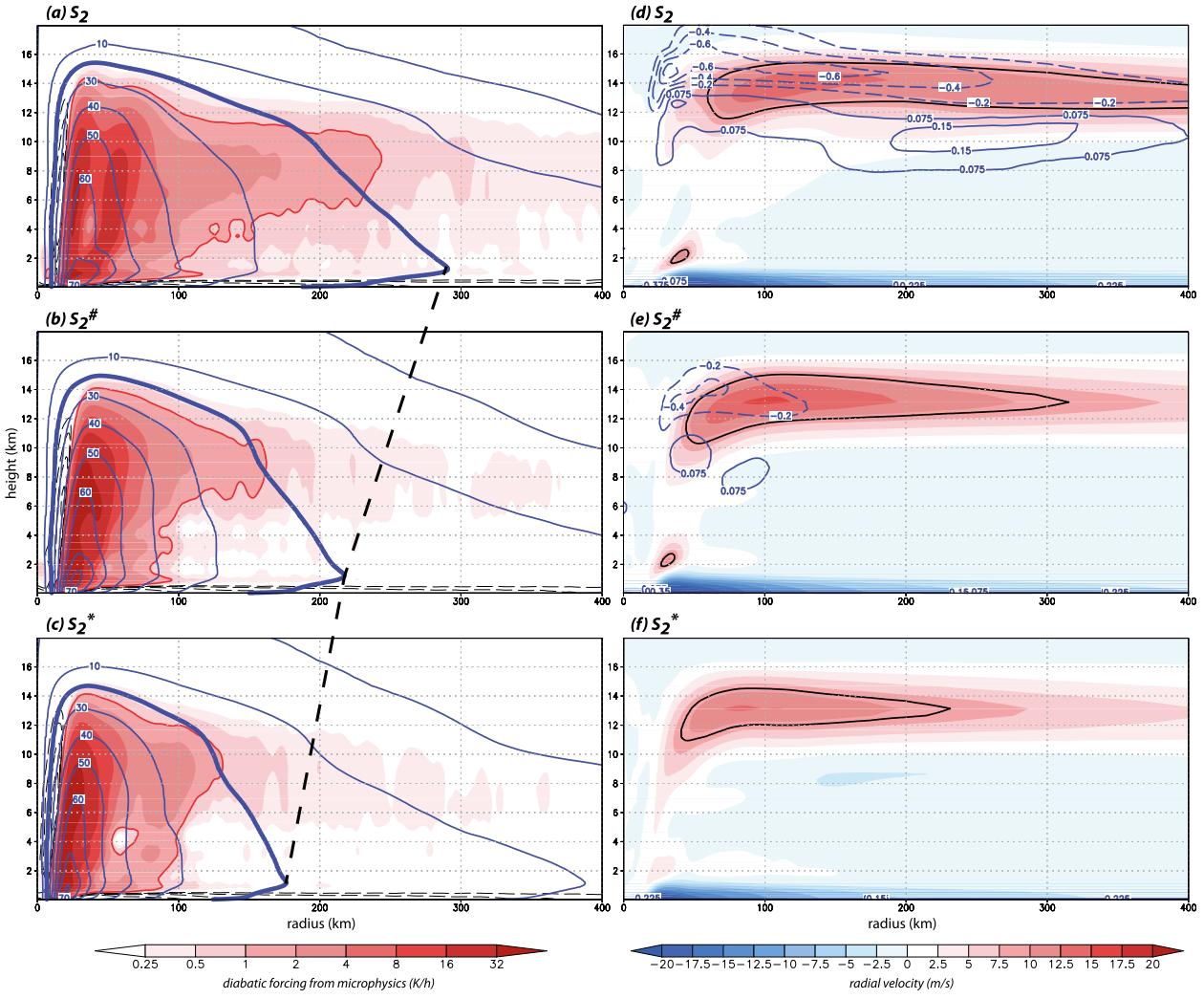

FIG. 11-16. Radius–height cross sections of (a)–(c) net diabatic heating from microphysics (shaded as shown, 1 K h^{-1} contour superposed) and tangential wind (20 m s^{-1} contour highlighted), and (d)–(f) radial wind (shaded as shown, 9 m s^{-1} contour superposed) and net radiation (contour intervals 0.2 and 0.075 K h^{-1} for negative and positive values, respectively) for three versions of the S_2 scheme. Each field represents the azimuthally symmetric components extracted from vortex-following composites constructed over the final 24 h.

and heating fields. An axisymmetric version of CM1 with 5-km radial resolution was used, and the simulations were integrated to maturity using a version of Thompson microphysics with the Goddard LW and SW schemes. Although some differences are apparent, which reflect alterations with respect to the model framework, initial sounding, and physical parameterizations, activating CRF is yet again found to widen the eye and enhance the secondary circulation, including the upper-level outflow (see P7's Fig. 9), and result in a substantially expanded wind field (Fig. 11-18). The net radiative forcing field is comparable in magnitude and spatial pattern to those from other models (Fig. 11-19a) despite the employment of a different radiation package. It is again seen that the condensation field is expanded when CRF is active (see difference field in Fig. 11-19c), which reinforces the association between CRF and enhanced convective activity in the outer core region.

While it is logical that the cloud-radiative forcing field is only as wide as the cloudy area, this does not mean CRF actively helped expand the anvil or winds. To address this, P7 introduced the ''CRF-fixed'' experiment (Fig. 11-19d) in which the time-dependent CRF field was replaced with the CRF-on run's temporal average, which was computed during maturity and over multiple diurnal cycles. The field was then introduced at the initial time and held constant during the integration, thereby rendering it independent of convective activity. The CRF-fixed simulation produced a cloud shield

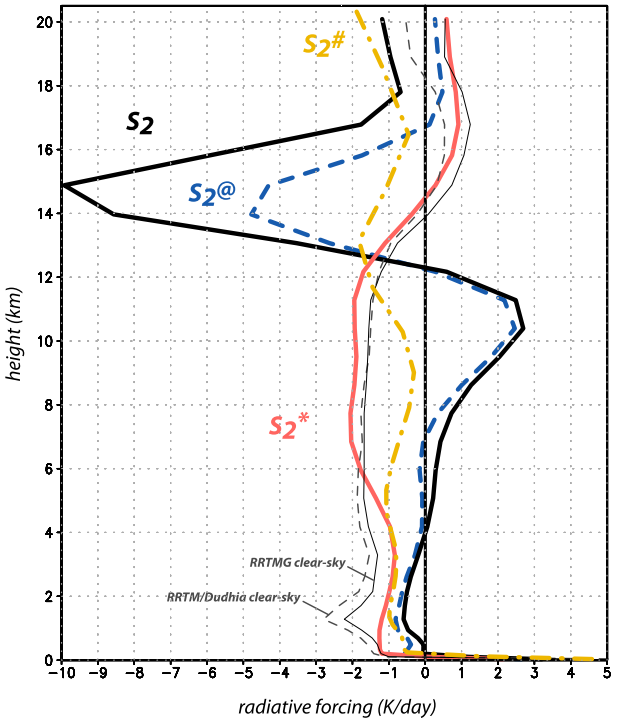

FIG. 11-17. Vertical profiles of net radiative forcing tendencies (K day^{-1}), averaged over a 350-km radius centered on the storm through a diurnal cycle, for four versions of S_2, along with the undisturbed clear-sky profiles for RRTMG and RRTM/Dudhia. In addition to CRF-on and CRF-off simulations with RRTM/Dudhia (S_2 and S_2^*), case $S_2^\#$ treats cloud ice as snow for LW calculations, and $S_2^@$ employed the RRTMG scheme.

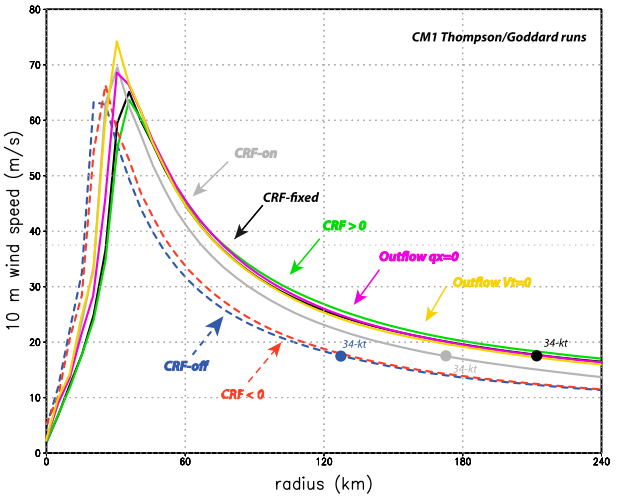

FIG. 11-18. Radial profiles of temporally averaged 10-m wind speed from CM1 experiments using Thompson MP and Goddard radiation and including CRF-on, CRF-off, and CRF-fixed cases. Simulations "CRF $\geq$ 0" and "CRF $\leq$ 0" are versions of CRF-fixed in which only the positive and negative CRF forcings were retained. Experiments "Outflow Vt = 0" and "Outflow qx = 0" are versions of CRF-fixed in which the terminal velocity and mixing ratio of hydrometeors in the outflow were set to zero, respectively. Radii of the 34-kt (17.5 m s^{-1}) wind are indicated. Averaged between days 9 and 12, inclusive. From P7.

(Fig. 11-19d) and tangential wind field (Fig. 11-18) that was comparable to the CRF-on case that supplied its radiative forcing (Fig. 11-19a).[10] Furthermore, the horizontal scale of the imposed CRF field can be altered arbitrarily, and the fact that the cloudy area directly responds to it (Fig. 11-20) clearly demonstrates that this relatively small diabatic forcing plays an integral role in determining anvil extent.

P7 also explored the direct and indirect impacts of CRF with a dry version of CM1 into which diabatic forcings from the moist experiments were inserted (Fig. 11-21). The dry model response to the full, temporally averaged CRF field was characterized by enhanced upper-tropospheric outflow (Fig. 11-21a), which may help explain why the CRF-active storms possessed stronger radial winds there. Note that the outflow also transports the very hydrometeors that cause the radiative forcing in the first place, so strengthening the outflow should lead to a progressively wider anvil, at least in the upper troposphere (depicted in Fig. 11-22). This scenario represents an apparent positive feedback process between the CRF and the radial outflow, and a fundamentally similar idea was explored by Krueger and Zuluaf (2002) and Durran et al. (2009).

At first, it was believed that the primary agent of the outflow enhancement would be the LW cooling at cloud top, as this is relatively larger in magnitude and possesses sharper horizontal and vertical gradients. Yet, P7 showed that the net cooling at cloud top played almost no role in the radial enhancement. The "CRF $<$ 0" version of the CRF-fixed experiment, which only retained the negative forcing, looks little different (Figs. 11-18 and 11-19e) from the case which neglected radiative forcing altogether (Fig. 11-19b). It is the subtle warming within the cloud shield, a consequence of the influence of hydrometeors on LW absorption and emission, that is relevant to the storm expansion, as demonstrated by the "CRF $>$ 0" experiment (Fig. 11-19f).

The dry model experiments of P7 also suggested that the in-cloud LW warming is primarily responsible for the enhanced outflow in the upper troposphere (Figs. 11-21b,c). The direct result of the positive CRF forcing is to produce very weak but deep and persistent ascent

[10] The radial extent of the anvil and wind actually exceeded that of the CRF-on TC during the period shown because the cloud-radiative forcing was applied from the initial time, while the CRF-on simulation required several days to achieve forcing of comparable spatial extent and magnitude.

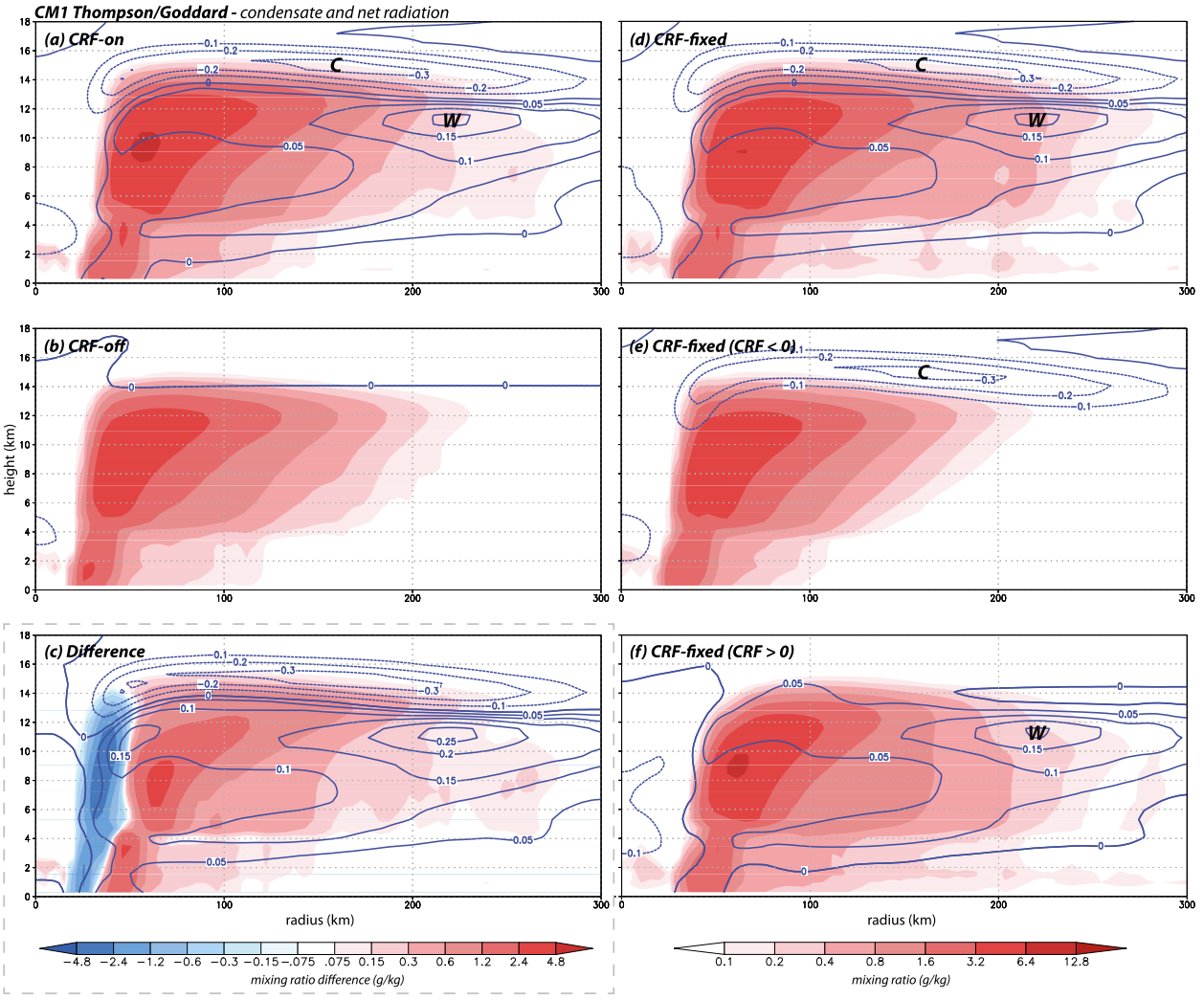

FIG. 11-19. Total condensate (shaded, note logarithmic scale) and net radiation [negative (dashed) contour interval 0.1 K h^{-1}, and positive (solid) interval 0.05 K h^{-1}] for CM1 Thompson/Goddard model storms, averaged as in Fig. 11-17: (a) CRF-on, (b) CRF-off, and (c) difference between CRF-on and CRF-off. At right, similar displays from members of the CRF-fixed experiment: (d) CRF-fixed, (e) CRF-fixed with only negative CRF forcing (CRF ≤ 0), and (f) CRF-fixed with only positive CRF forcing (CRF ≥ 0). Letters "*C*" and "*W*" highlight local maxima of diabatic cooling and warming, respectively. In (c), the color legend at bottom left is used; other panels use the bottom-right legend. From P7.

throughout the cloud shield (Fig. 11-21d). In a two-dimensional but slab-symmetric geometry, such concentrated rising motion could be expected to result in some amount of flow directed away from the heat source in both horizontal directions. In this axisymmetric framework, however, inertial stability strongly resists inward radial displacements (e.g., Eliassen 1951; Shapiro and Willoughby 1982; Holland and Merrill 1984), and thus the radial wind response is strongly biased toward outflow. The LW cooling at cloud top may be more extensive than the in-cloud LW warming, but it also occupies a much smaller volume. Vertically extensive, if gentle, ascent accomplishes the upward mass transport necessary to enhance upper-tropospheric outflow of appreciable magnitude.

It was also initially believed that the enhanced upper-tropospheric radial outflow associated with CRF, whether responding to LW cooling or warming or some combination thereof, was directly responsible for enabling the enhanced outer region convection, with the concomitant radial broadening of the tangential wind field. We hypothesized (in P4) that outward transport of hydrometeors not only provided the aforementioned positive feedback but also, through fallout and subsequent reconversion to vapor, helped moisten the outer core, eventually rendering it more conducive to the convective

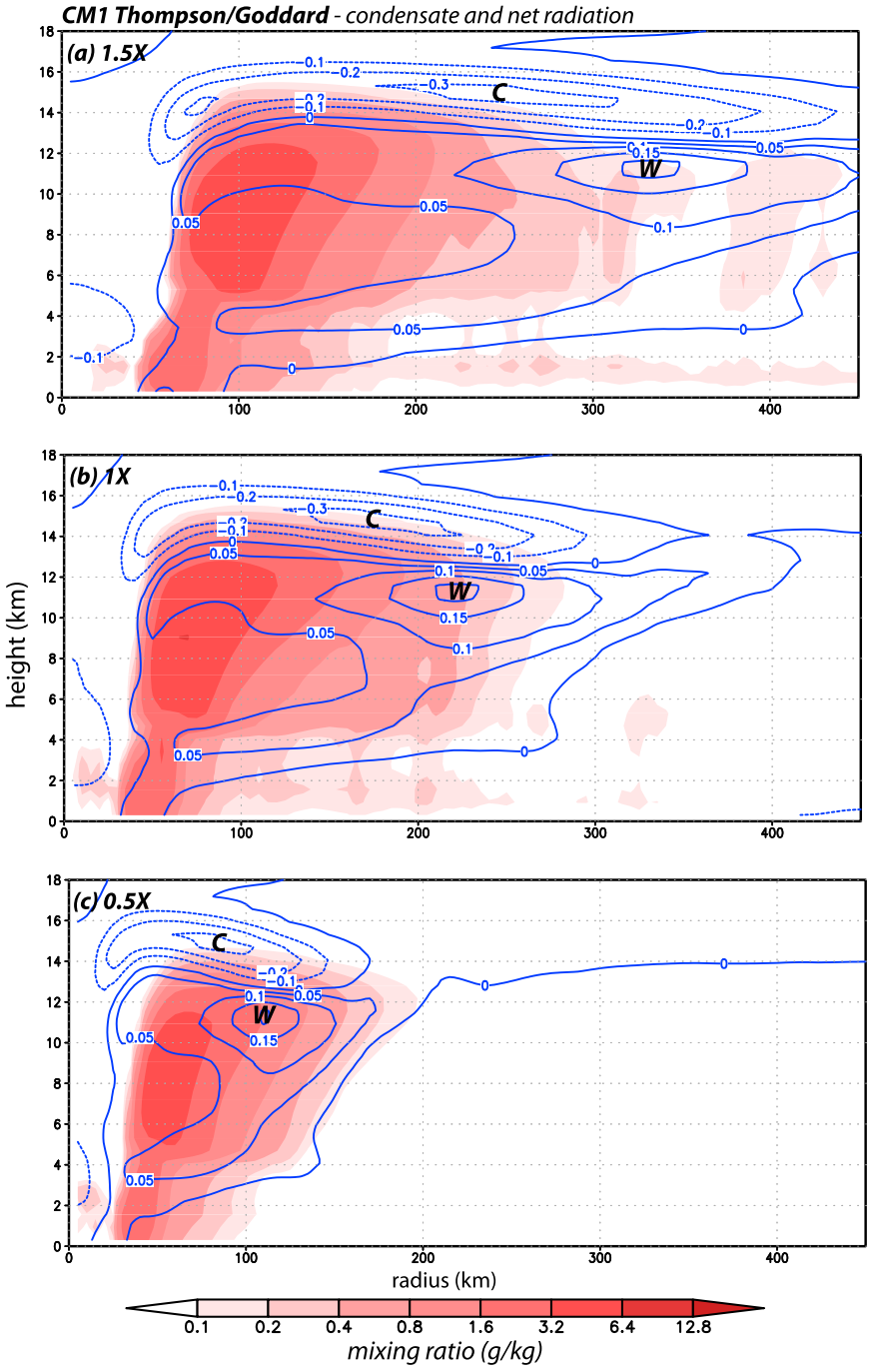

FIG. 11-20. As in Fig. 11-19d, but with the horizontal scale of the imposed CRF field varied from (a) 1.5 times, (b) 1.0 times, and (c) 0.5 times the original radial extent employed in the CRF-fixed simulation. Note the horizontal domain area shown has been increased to 450 km.

activity (see Fig. 11-22) that has been associated with broader wind fields. As the convective activity expanded outward, upward mass transport associated with it helped further augment and expand the upper-tropospheric outflow, and transport even more hydrometeors farther outward. This is another positive feedback leading to storm expansion with respect to the anvil and winds.

This proposed explanation was tested (in P7) by artificially interfering with the radial transport of hydrometeors in the upper-tropospheric outflow. In the

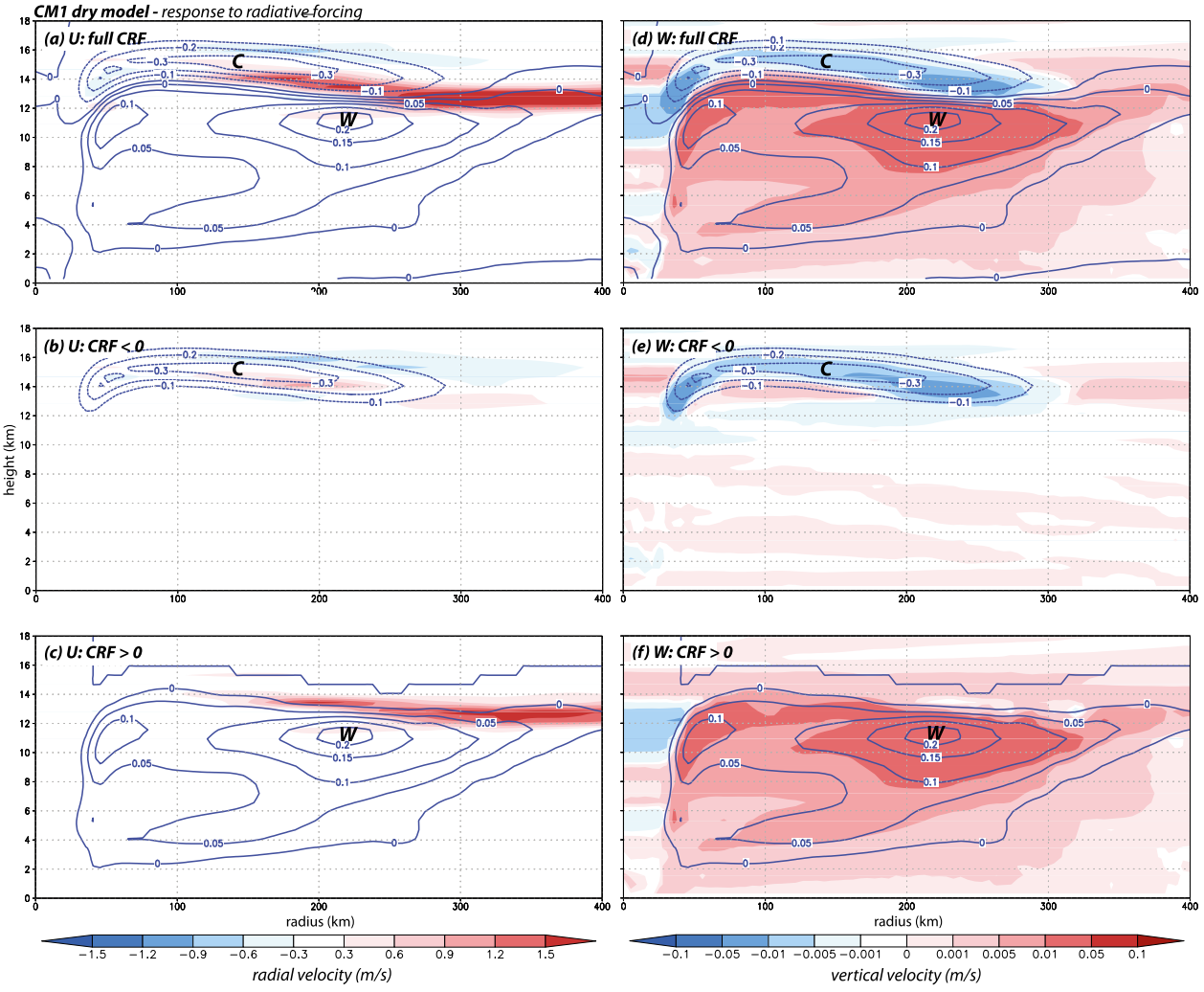

FIG. 11-21. Simulations from the dry version of CM1 forced by the difference between the CRF-on storm cloudy and clear-sky radiative tendencies (contoured as in Fig. 11-16d) averaged between days 9 to 12, inclusive. Radial velocity (shaded) response for the (a) full CRF forcing field, (b) CRF ≤ 0 component, and (c) CRF ≥ 0 component. Vertical velocity (shaded) response for the (d) full CRF forcing field, (e) CRF ≤ 0 component, and (f) CRF ≥ 0 component. Dry fields are averaged over the simulations first 4 days. From P7.

experiment "Outflow Vt = 0", condensation particles within the outflow beyond the radius of maximum wind (RMW) were given zero terminal velocity, which prevented them from easily settling into the dry midtropospheric region below the anvil shield. This restriction did not prevent convective activity (not shown) and the development of a wind field comparably broad to the CRF-on TC (Fig. 11-18). Forcing complete removal of hydrometeors within the radial outflow (experiment "Outflow qx = 0" in Fig. 11-18) also failed to prevent the development of a materially wider storm.

Thus, P7 concluded that the primary agent for inducing the convective activity was the very weak but deep and persistent ascent produced by the LW warming throughout the cloud shield (Fig. 11-21d). Its direct effect is to lift, very gently, air parcels toward their saturation points. Once saturation is achieved in a particular area, the much larger diabatic forcings associated with vapor phase changes and other microphysical processes can establish and sustain the enhanced outer-core convective activity that characterizes CRF-active simulations with enhanced diabatic heating and/or more extensive deep cloudiness (Figs. 11-16 and 11-19).

P7 completed this picture by linking the more extensive convective heating and the tangential wind field broadening. The extra diabatic heating generated in the outer region in the CRF-on TC was inserted in the dry model, which produced a circulation that directly enhanced the cyclonic winds beneath and radially outward from the heat source (see P7's Fig. 14). This response is

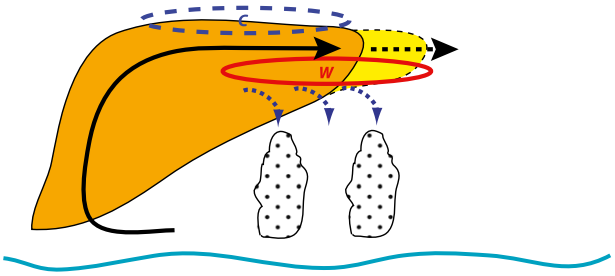

FIG. 11-22. Hypothesis for anvil self-spreading due to cloud-radiative processes, and presumed influence on outer convective activity advanced in P4 and largely refuted in P7. CRF associated with the cloudy area (depicted in orange) results in radial expansion (dashed black line) of the secondary circulation (solid black line), directly extending the cloudy area (depicted in yellow), which leads to expansion of the CRF field as well as hydrometeor fallout (blue dotted lines) that moistens the outer core, and thus was believed to eventually lead to enhanced convection (dotted area). Adapted from P4.

again due to the inertial stability distribution and could have been anticipated from prior work with Sawyer–Eliassen models (e.g., Shapiro and Willoughby 1982; Hack and Schubert 1986). Therefore, it is suggested that the in-cloud CRF warming directly results in lifting that, as a consequence of the enhanced convective activity it encourages, indirectly causes the anvil and wind field expansion in those simulated TCs that incorporate some measure of opaque clouds.

Finally, we note that although CRF provides one avenue for broadening the wind profile, it remains that even "cloudy" idealized and semi-idealized TCs often appear to be too radially compact relative to actual storms, especially in high-resolution simulations. This tendency becomes more obvious when the temporally and azimuthally averaged 700-hPa wind profiles are normalized with respect to the maximum tangential wind (V_m) and the RMW (R_m), as shown for simulations S_2, S_2^*, and $S_2^\#$ in Fig. 11-23a. Nondimensionalization essentially discounts the influence of eye size on outer wind strength. Also shown are modified Rankine (MR) wind profiles (cf. Depperman 1947; Anthes 1982), given by

$$\frac{V}{V_m} = \left(\frac{R}{R_m}\right)^{\alpha}, \qquad (11\text{-}3)$$

with decay (shape) parameters set to $\alpha = 0.5$, 0.625, and 0.75. This is one of a number of outer wind profile functions that have been proposed (e.g., Holland 1980; DeMaria 1987; Willoughby et al. 2006).

Mallen et al. (2005) analyzed flight-level (largely 700 hPa) data from 72 major hurricanes[11] and found values of $0.18 \le \alpha \le 0.67$, with an average of $\alpha = 0.48$, for the interval $1 \le R/R_m \le 3$. Over that range, the wind profiles of storms S* and $S_2^\#$ are very well described by MR profiles with $\alpha = 0.75$, which exceeds the largest decay parameters from the Mallen et al. (2005) survey. Even in the S_2 case, which has the broadest (nondimensional) outer wind profile among the WRF-ARW TCs, the winds decayed with radius more rapidly than a substantial majority of the 72 cases. Similar compact wind profiles are found with HWRF simulations made for P7's study (Fig. 11-23b). In P5, we demonstrated that the outer wind structure also could also reflect model physics such as microphysics more so than the initial profile, even though bogussed vortices appeared to be resilient.

d. Global extension of the CRF experiment

Typically, several days are required for TCs to reach maturity in idealized and semi-idealized simulations, even when initialized with bogussed circulations. This prolonged evolution represents a significant shortcoming in the semi-idealized approach, which utilizes the real-data framework employed in operations. Real-data simulations require boundary tendencies from a "parent" model to guide how the regional-scale model's atmosphere evolves. In this semi-idealized situation, there is no parent—the bogus or bubble is placed in an otherwise horizontally homogeneous atmosphere—so those tendencies are zero, effectively sealing the model domain. This limits how long the simulations can be integrated as boundary influences eventually become important. Given the domain sizes employed, running for four days is acceptable, but longer simulations become problematic. The issue is the model storms generally have not finished intensifying prior to the end of these simulations.

A global model would permit longer integrations, but the required high resolution would come with a significant computational cost. As a pilot study, the global MPAS model is used with a variable-resolution, 163 842-cell mesh with coarse grid spacing of 92 km that is refined to 25 km over a circular area of roughly 30° latitude in radius, and with 41 vertical levels (see Table 11-1). A variety of bubble-initialized simulations were made using W6 microphysics with and without convective parameterization employed following the spinup period. For this example, the MP scheme was active from the initial time and the Kain–Fritsch convective scheme was switched off at the 48-h mark. Model runs extended over nine full days, during which time the TC cores remained comfortably within the refinement region. Other experiments yielded TCs that were quantitatively, but not qualitatively, different.

[11] Category 3 or higher on the Saffir–Simpson scale, based on the 10-m wind speed.

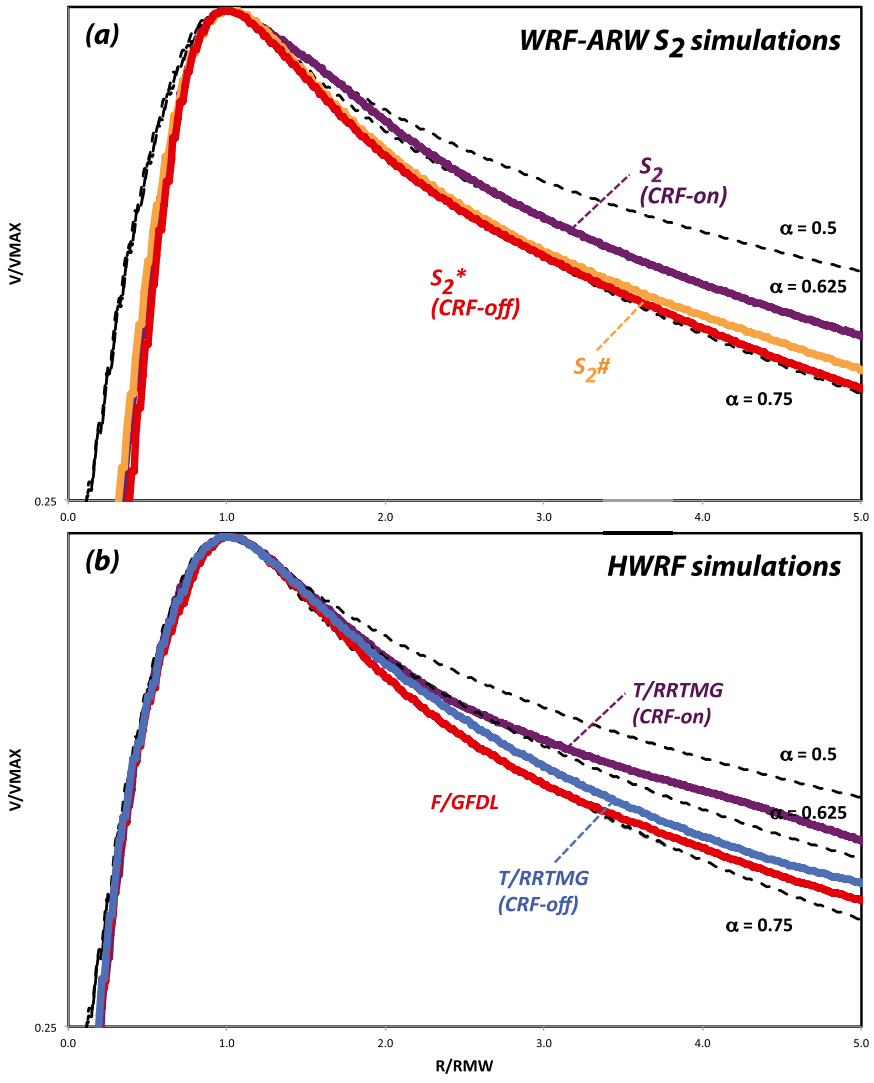

FIG. 11-23. Time-averaged symmetric component of 700-hPa tangential wind speed, non-dimensionalized with respect to maximum wind (V_{max}) and radius of maximum wind (RMW or R_m), along with modified Rankine profiles using values of $\alpha = 0.5$, 0.625, and 0.75 in (11-3). Compare with P5's Fig. 9c.

Both the CRF-on and CRF-off storms appear to have reached maturity around 4–5 days, at least with respect to maximum 10-m wind speed and minimum SLP (Fig. 11-24). After a delay on the order of 12–24 h, the CRF-off storm attained roughly the same wind speeds seen in the "cloudy" counterpart, which corresponds to Saffir–Simpson category 1. Storm intensity is restrained by the coarse horizontal resolution and by the absence of the convective parameterization after spinup, although leaving the Kain–Fritsch scheme on only permits the storms to edge into category 2 (not shown). Averaged over the ninth day, the tangential wind field on the TCs' eastern flanks is clearly more radially extensive in the "cloudy" case and the MP forcing is also substantially wider (Fig. 11-25), which is consistent with results from the regional model simulations.

In contrast with the regional simulations, the wind fields for these MPAS TCs are extremely broad by the end of the simulations, with 34-kt wind radii extending beyond 300 km (not shown, but it can be inferred from Fig. 11-25). This is in part a consequence of the coarse (25 km) resolution. Owing to the strength of these outer winds, the rapid northwestward motions of the MPAS TCs (compared to other bubble-initialized storms) are not surprising (Fig. 11-26). However, the relatively faster winds in the CRF-active case give this TC an even more substantial beta drift, and by the end of the ninth day this TC has translated over 330 km farther than the

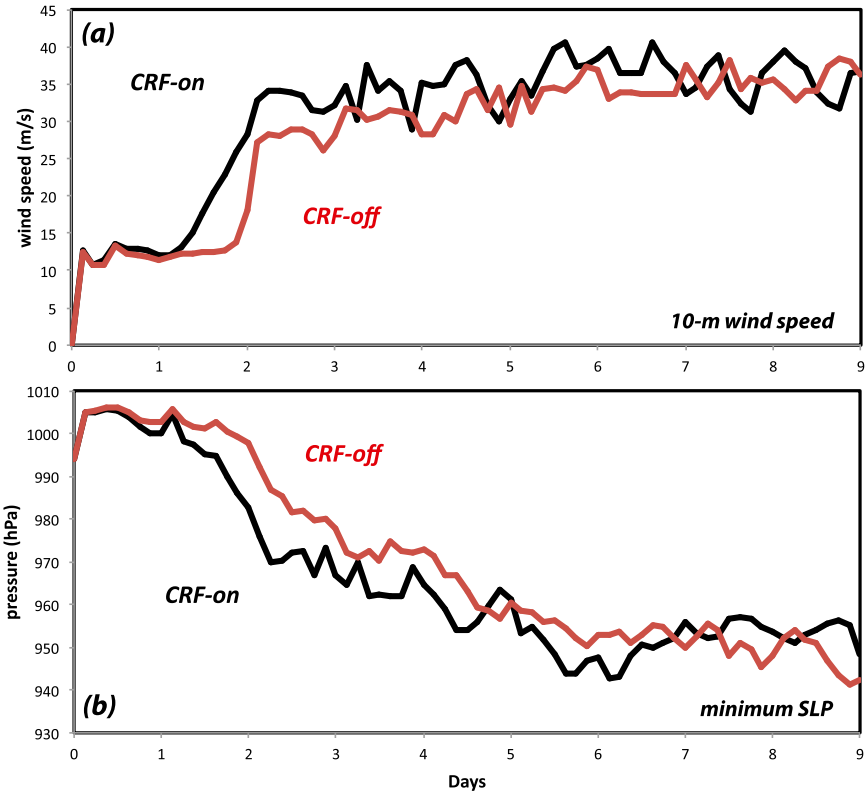

FIG. 11-24. Time series of domain (a) maximum 10-m wind speed and (b) minimum SLP from 9-day MPAS simulations with and without CRF.

transparent-cloud counterpart (Fig. 11-26). The translation speed difference between the two increases sharply after the fourth day of integration. While higher-resolution simulations should be attempted in the future, the principal results from the regional experiments have been verified in a global model with a less restrictive physical framework.

5. Summary

This paper surveyed a body of work (referred to as papers P1–P7; see Table 11-1) that focused on the influences that cloud microphysical processes can have on aspects of tropical cyclones (TCs) other than intensity. High-resolution simulations with semi-idealized and idealized numerical models were made, many of which employed a bubble initialization in which the cyclone was bred from a synoptic-scale buoyancy perturbation as an alternative to the imposition of artificially constructed bogus vortices. The TC characteristics of interest included the track, magnitude, and spatial extent of the radial and tangential winds, asymmetries with respect to the inner-core diabatic heating, convective activity through the outer rainband region, and the evolution and extent of the TC anvil cloud. To a large degree these characteristics are sensitive to the microphysical parameterization (MP) owing to the interaction of hydrometeors with radiation, which we termed the cloud-radiative forcing (CRF).

In the absence of environmental steering, TC motion reflects a combination of beta drift and convective heating variations responding in part to beta-induced asymmetries (the beta shear). The beta drift is caused by a ventilation flow across the vortex that is generated as a consequence of differential advection of planetary vorticity on a curved Earth, and depends on the outer wind strength. Microphysical assumptions were shown to directly and indirectly modulate the strength of these winds, which result in motion variations with respect to both speed and direction (P1–P3). The beta shear is due to the warm core nature of the TC and encourages the development of asymmetric diabatic heating structures. These heating asymmetries, which are particularly important in the bubble-initialized model storms that incorporated ice microphysics, subtly but powerfully alter storm motion depending on the orientation of the asymmetry pattern, which varied from one MP to another.

In contrast, simulations with warm rain (Kessler) microphysics and/or bogussed vortices were more resilient,

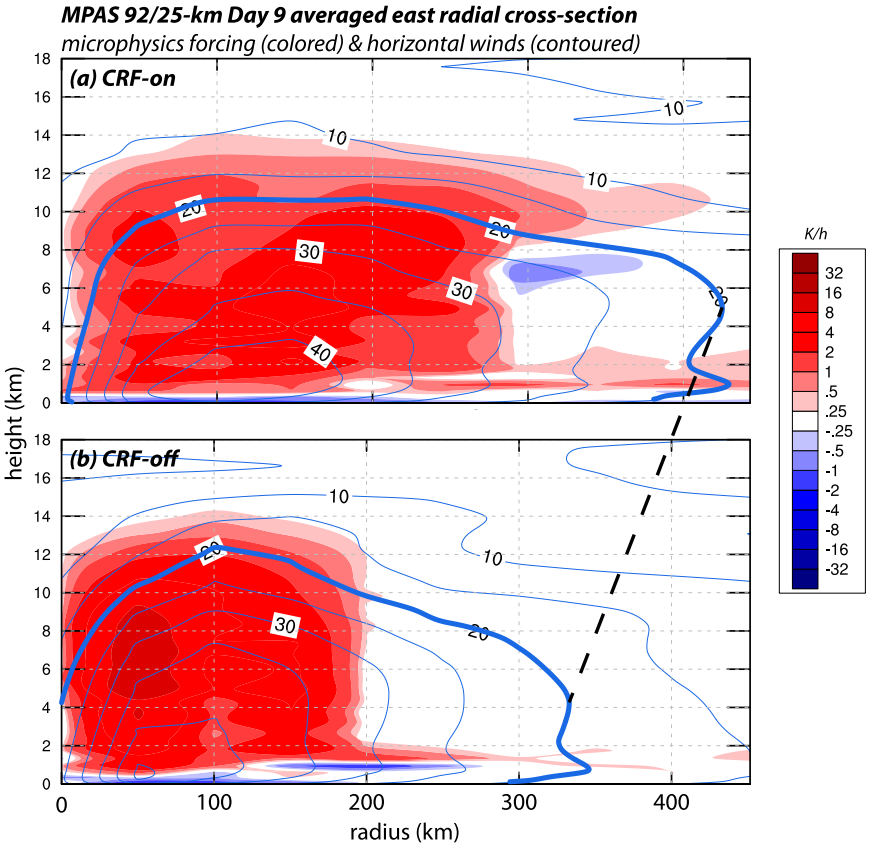

FIG. 11-25. Time-averaged fields of horizontal wind (5 m s^{-1} contours) and diabatic heating from microphysics (shaded) for (a) CRF-on and (b) CRF-off MPAS simulations. This cross section is computed following the vortex and averaged over the ninth day to represent structures that extend eastward from the storm center, and have not been azimuthally averaged.

successfully resisting the development of asymmetries (P5), at least until they were imposed on the storm by the environment, such as through the interaction of the TC with a topographic obstacle (P6). Without the development of asymmetric heating structures that tended to oppose the beta drift, relatively rapid translation was simulated and diagnosed. This was revealed through potential vorticity analyses applied to time-averaged, vortex-following composites (P3 and P5–P7). The realism of these symmetric and asymmetric structures deserves closer examination.

Variations among bubble-initialized model storms with respect to tracks, asymmetric convective patterns, and anvil extents largely vanished when the cloud-radiative forcing was removed in the aquaplanet model (P3). The various MPs produce different amounts, types, and distributions of particles, and ostensibly impact storm dynamics or thermodynamics through LW absorption and emission and SW absorption in a manner that depends largely on particle size (and thus species). Simulated storms with active CRF tended to have larger eyes, more widespread convective activity in the outer region, and faster outer-core winds relative to their CRF-off counterparts (P3, P7). The CRF-on storms also possessed stronger secondary circulations with faster radial inflow at the lowest levels and stronger outflow aloft, and thicker and more radially extensive anvils. The bubble-initialized warm rain TC became quite symmetric because the effects of CRF were exaggerated by the huge radiative forcing associated with tiny cloud droplets.

Although the LW warming within the anvil is weak, it is the most significant component of CRF as it leads directly to stronger upper-tropospheric radial outflow as well as slow, yet sustained, ascent throughout the outer core (P7). This gentle ascent results in a moistening of the region outside the eyewall, enhances convective activity, elevates the equivalent potential temperature, and increases the radial extent of the TC, including its anvil and wind fields. These conclusions were reinforced with dry model experiments that examined in isolation the roles played by diabatic heat sources. The net heating associated with increased convection in the outer region directly acts to

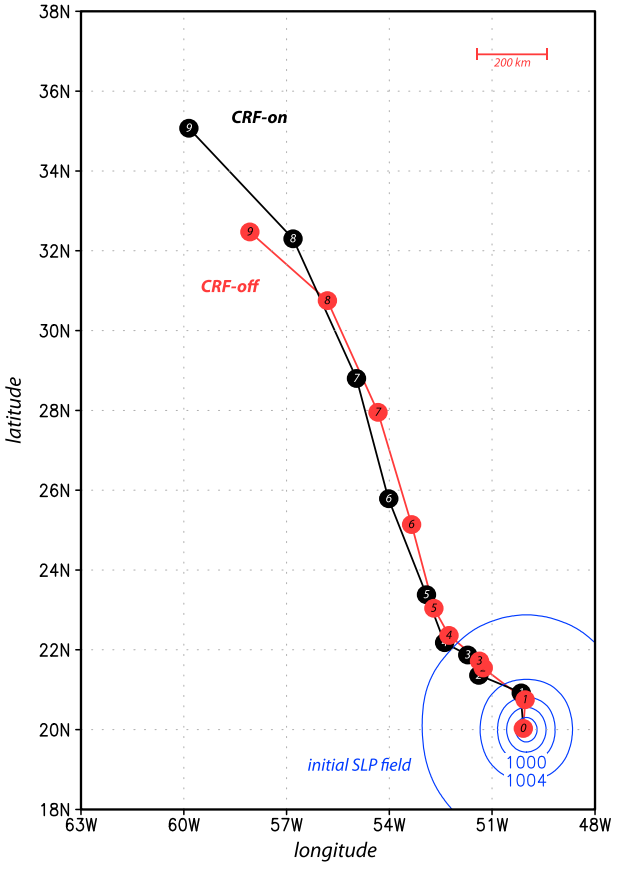

FIG. 11-26. Tracks from 9-day MPAS simulations for CRF-on (black) and CRF-off (red) storms. Day number indicated in position circles. Initial SLP field is shown in blue (4-hPa contours).

intensify both the cyclonic winds in the lower troposphere and the secondary circulation.

Finally, some semi-idealized simulations made with the global MPAS model were used to examine the influence of CRF on TC motion and structure within longer integrations without the limitations imposed by lateral boundary conditions required in regional models. Although the MPAS spatial resolution employed is rather coarse, these experiments confirmed that CRF acts to enhance convective activity in the outer region and broaden the wind profile, which lead to potentially different motions and hazards (e.g., as outer winds influence storm surges). In summary, the assumptions inherent in cloud microphysical parameterizations represent important contributions to forecast uncertainty, particularly because they are amplified by the role radiative processes can play in nontransparent clouds.

Acknowledgments. Professor Michio Yanai was a strong supporter and source of inspiration for this work. Drs. Kevin Hill and Gary Lackmann inspired the semi-idealized framework and the bubble initialization. Dr. Axel Seifert kindly lent us his two-moment microphysics scheme, and Dr. George Bryan permitted use of his CM1 model. WRF-ARW and HWRF analyses employed a customized version of the RIP package, created by Dr. Mark Stoelinga. We thank Dr. Bill Skamarock and Mr. Michael Duda for MPAS support, and Mr. Omar Nava for assisting with development of MPAS analysis tools. The authors also thank Drs. Kuo-nan Liou, Russ Elsberry, Gregory Thompson, Ligia Bernardet, Brad Ferrier, Mrinal Biswas, Yu Gu, Longtao Wu, and Mr. Donald Boucher for information, important interactions, and encouragement. Suggestions from two reviewers are gratefully acknowledged. Portions of this work were supported by the National Science Foundation (ATM-0554765), a Jet Propulsion Laboratory Strategic University Research Partnership grant, the Aerospace Corporation, the National Science Council and Central Weather Bureau of Taiwan, the National Atmospheric and Oceanic Administration's Hurricane Forecast Improvement Program (HFIP; NA12NWS4680009), and the National Aeronautics and Space Administration's Hurricane Science Research Program (HSRP; NNX12AJ83G).

REFERENCES

Anthes, R. A., 1982: *Tropical Cyclones: Their Evolution, Structure and Effects. Meteor. Monogr.*, No. 41, Amer. Meteor. Soc., 298 pp.

Bender, M., 1997: The effect of relative flow on the asymmetric structure in the interior of hurricanes. *J. Atmos. Sci.*, **54**, 703–724, doi:10.1175/1520-0469(1997)054<0703:TEORFO>2.0.CO;2.

Bryan, G. H., and M. Fritsch, 2002: A benchmark simulation for moist nonhydrostatic numerical models. *Mon. Wea. Rev.*, **130**, 2917–2928, doi:10.1175/1520-0493(2002)130<2917:ABSFMN>2.0.CO;2.

Bu, Y., 2012: Factors that can influence the onset time of rapid intensification of tropical cyclones. M.S. thesis, Atmospheric and Oceanic Sciences, University of California, Los Angeles, 75 pp.

——, R. G. Fovell, and K. L. Corbosiero, 2014: Influence of cloud-radiative forcing on tropical cyclone structure. *J. Atmos. Sci.*, **71**, 1644–1662, doi:10.1175/JAS-D-13-0265.1.

Cao, Y., R. G. Fovell, and K. L. Corbosiero, 2011: Tropical cyclone track and structure sensitivity to initialization in idealized simulations: A preliminary study. *Terr. Atmos. Ocean. Sci.*, **22**, 559–578, doi:10.3319/TAO.2011.05.12.01(TM).

Chan, J. C.-L., and R. T. Williams, 1987: Analytical and numerical studies of the beta-effect in tropical cyclone motion. *J. Atmos. Sci.*, **44**, 1257–1265, doi:10.1175/1520-0469(1987)044<1257:AANSOT>2.0.CO;2.

Chen, S.-H., and W.-Y. Sun, 2002: A one-dimensional time dependent cloud model. *J. Meteor. Soc. Japan*, **80**, 99–118, doi:10.2151/jmsj.80.99.

Chou, M. D., and M. J. Suarez, 1994: An efficient thermal infrared radiation parameterization for use in general circulation models. NASA Tech. Memo. 104606, 85 pp.

Collins, W. D., and Coauthors, 2006: The formulation and atmospheric simulation of the Community Atmosphere Model version 3 (CAM3). *J. Climate*, **19**, 2144–2161, doi:10.1175/JCLI3760.1.

Corbosiero, K. L., and J. Molinari, 2002: The effects of vertical wind shear on the distribution of convection in tropical cyclones. *Mon. Wea. Rev.*, **130**, 2110–2123, doi:10.1175/1520-0493(2002)130<2110:TEOVWS>2.0.CO;2.

DeMaria, M., 1987: Tropical cyclone track prediction with a barotropic spectral model. *Mon. Wea. Rev.*, **115**, 2346–2357, doi:10.1175/1520-0493(1987)115<2346:TCTPWA>2.0.CO;2.

Depperman, C. E., 1947: Notes on the origin and structure of Philippine typhoons. *Bull. Amer. Meteor. Soc.*, **28**, 399–404.

Dudhia, J., 1989: Numerical study of convection observed during the Winter Monsoon Experiment using a mesoscale two-dimensional model. *J. Atmos. Sci.*, **46**, 3077–3107, doi:10.1175/1520-0469(1989)046<3077:NSOCOD>2.0.CO;2.

——, S.-Y. Hong, and K.-S. Lim, 2008: A new method for representing mixed-phase particle fall speeds in bulk microphysics parameterizations. *J. Meteor. Soc. Japan*, **86A**, 33–44, doi:10.2151/jmsj.86A.33.

Durran, D. R., T. Dinh, M. Ammerman, and T. Ackerman, 2009: The mesoscale dynamics of thin tropical tropopause cirrus. *J. Atmos. Sci.*, **66**, 2859–2873, doi:10.1175/2009JAS3046.1.

Eliassen, A., 1951: Slow thermally or frictionally controlled meridional circulation in a circular vortex. *Astrophys. Norv.*, **5**, 19–60.

Ferrier, B. S., Y. Jin, T. Black, E. Rogers, and G. DiMego, 2002: Implementation of a new grid-scale cloud and precipitation scheme in NCEP Eta model. *15th Conf. on Numerical Weather Prediction*, San Antonio, TX, Amer. Meteor. Soc., 280–283. [Available online at https://ams.confex.com/ams/SLS_WAF_NWP/techprogram/paper_47241.htm.]

Fiorino, M. J., and R. L. Elsberry, 1989: Some aspects of vortex structure related to tropical cyclone motion. *J. Atmos. Sci.*, **46**, 975–990, doi:10.1175/1520-0469(1989)046<0975:SAOVSR>2.0.CO;2.

Fovell, R. G., and H. Su, 2007: Impact of cloud microphysics on hurricane track forecasts. *Geophys. Res. Lett.*, **34**, L24810, doi:10.1029/2007GL031723.

——, K. L. Corbosiero, and H.-C. Kuo, 2009: Cloud microphysics impact on hurricane track as revealed in idealized experiments. *J. Atmos. Sci.*, **66**, 1764–1778, doi:10.1175/2008JAS2874.1.

——, ——, and ——, 2010a: Influence of cloud-radiative feedback on tropical cyclone motion: Symmetric contributions. *29th Conf. on Hurricanes and Tropical Meteorology*, Tucson, AZ, Amer. Meteor. Soc., 13C.5. [Available online at https://ams.confex.com/ams/pdfpapers/168859.pdf.]

——, ——, A. Seifert, and K.-N. Liou, 2010b: Impact of cloud-radiative processes on hurricane track. *Geophys. Res. Lett.*, **37**, L07808, doi:10.1029/2010GL042691.

Frank, W. M., and E. A. Ritchie, 1999: Effects of environmental flow upon tropical cyclone structure. *Mon. Wea. Rev.*, **127**, 2044–2061, doi:10.1175/1520-0493(1999)127<2044:EOEFUT>2.0.CO;2.

Fu, Q., and K. N. Liou, 1993: Parameterization of the radiative properties of cirrus clouds. *J. Atmos. Sci.*, **50**, 2008–2025, doi:10.1175/1520-0469(1993)050<2008:POTRPO>2.0.CO;2.

Gopalakrishnan, S. G., S. Goldenberg, T. Quirino, X. Zhang, F. Marks Jr., K.-S. Yeh, R. Atlas, and V. Tallapragada, 2012: Toward improving high-resolution numerical hurricane forecasting: Influence of model horizontal grid resolution, initialization, and physics. *Wea. Forecasting*, **27**, 647–666, doi:10.1175/WAF-D-11-00055.1.

Gu, Y., K. N. Liou, W. Chen, and H. Liao, 2010: Direct climate effect of black carbon in China and its impact on dust storms. *J. Geophys. Res.*, **115**, D00K14, doi:10.1029/2009JD013427.

——, ——, S. C. Ou, and R. G. Fovell, 2011: Cirrus cloud simulations using WRF with improved radiation parameterization and increased vertical resolution. *J. Geophys. Res.*, **116**, D06119, doi:10.1029/2010JD014574.

Hack, J. J., and W. H. Schubert, 1986: Nonlinear response of atmospheric vortices to heating by organized cumulus convection. *J. Atmos. Sci.*, **43**, 1559–1573, doi:10.1175/1520-0469(1986)043<1559:NROAVT>2.0.CO;2.

Hausman, S. A., K. V. Ooyama, and W. H. Schubert, 2006: Potential vorticity structure of simulated hurricanes. *J. Atmos. Sci.*, **63**, 87–108, doi:10.1175/JAS3601.1.

Hill, K. A., and G. M. Lackmann, 2009: Influence of environmental humidity on tropical cyclone size. *Mon. Wea. Rev.*, **137**, 3294–3315, doi:10.1175/2009MWR2679.1.

Holland, G. J., 1980: An analytic model of the wind and pressure profiles in hurricanes. *Mon. Wea. Rev.*, **108**, 1212–1218, doi:10.1175/1520-0493(1980)108<1212:AAMOTW>2.0.CO;2.

——, 1983: Tropical cyclone motion: Environmental interaction plus a beta effect. *J. Atmos. Sci.*, **40**, 328–342, doi:10.1175/1520-0469(1983)040<0328:TCMEIP>2.0.CO;2.

——, and R. T. Merrill, 1984: On the dynamics of tropical cyclone structural changes. *Quart. J. Roy. Meteor. Soc.*, **110**, 723–745, doi:10.1002/qj.49711046510.

Hong, S.-Y., J. Dudhia, and S.-H. Chen, 2004: A revised approach to ice microphysical processes for the bulk parameterization of clouds and precipitation. *Mon. Wea. Rev.*, **132**, 103–120, doi:10.1175/1520-0493(2004)132<0103:ARATIM>2.0.CO;2.

——, Y. Noh, and J. Dudhia, 2006: A new vertical diffusion package with an explicit treatment of entrainment processes. *Mon. Wea. Rev.*, **134**, 2318–2341, doi:10.1175/MWR3199.1.

Hsu, L.-H., H.-C. Kuo, and R. G. Fovell, 2013: On the geographic asymmetry of typhoon translation speed across the mountainous island of Taiwan. *J. Atmos. Sci.*, **70**, 1006–1022, doi:10.1175/JAS-D-12-0173.1.

Iacono, M. J., J. S. Delamere, E. J. Mlawer, M. W. Shephard, S. A. Clough, and W. D. Collins, 2008: Radiative forcing by long-lived greenhouse gases: Calculations with the AER radiative transfer models. *J. Geophys. Res.*, **113**, D13103, doi:10.1029/2008JD009944.

Jordan, C. L., 1958: Mean soundings for the West Indies area. *J. Meteor.*, **15**, 91–97, doi:10.1175/1520-0469(1958)015<0091:MSFTWI>2.0.CO;2.

Kessler, E., 1969: *On the Distribution and Continuity of Water Substance in Atmospheric Circulations*. *Meteor. Monogr.*, Amer. Meteor. Soc., No. 32, 84 pp.

Krueger, S. K., and M. A. Zuluaf, 2002: Radiatively-induced anvil spreading. *Proc. 15th ARM Science Team Meeting*, Daytona Beach, FL, Department of Energy, 280–283.

Li, X., and Z. Pu, 2008: Sensitivity of numerical simulation of early rapid intensification of Hurricane Emily (2005) to cloud microphysical and planetary boundary layer parameterizations. *Mon. Wea. Rev.*, **136**, 4819–4838, doi:10.1175/2008MWR2366.1.

Lin, Y. L., R. D. Farley, and H. D. Orville, 1983: Bulk parameterization of the snow field in a cloud model. *J. Climate Appl. Meteor.*, **22**, 1065–1092, doi:10.1175/1520-0450(1983)022<1065:BPOTSF>2.0.CO;2.

Liou, K. N., 2002: *An Introduction to Atmospheric Radiation.* 2nd ed. Academic Press, 583 pp.

Lord, S. J., H. E. Willoughby, and J. M. Piotrowicz, 1984: Role of a parameterized ice-phase microphysics in an axisymmetric,

nonhydrostatic tropical cyclone model. *J. Atmos. Sci.*, **41**, 2836–2848, doi:10.1175/1520-0469(1984)041<2836:ROAPIP>2.0.CO;2.

Mallen, K. J., M. T. Montgomery, and B. Wang, 2005: Re-examining the near-core radial structure of the tropical cyclone primary circulation: Implications for vortex resiliency. *J. Atmos. Sci.*, **62**, 408–425, doi:10.1175/JAS-3377.1.

Marshall, J. S., and W. M. Palmer, 1948: The distribution of raindrops with size. *J. Meteor.*, **5**, 165–166, doi:10.1175/1520-0469(1948)005<0165:TDORWS>2.0.CO;2.

McFarquhar, G. M., and R. A. Black, 2004: Observations of particle size and phase in tropical cyclones: Implications for mesoscale modeling of microphysical processes. *J. Atmos. Sci.*, **61**, 422–439, doi:10.1175/1520-0469(2004)061<0422:OOPSAP>2.0.CO;2.

——, H. Zhang, G. Heymsfield, R. Hood, J. Dudhia, J. B. Halverson, and F. Marks, 2006: Factors affecting the evolution of Hurricane Erin (2001) and the distributions of hydrometeors: Role of microphysical processes. *Mon. Wea. Rev.*, **136**, 127–150, doi:10.1175/JAS3590.1.

Mlawer, E. J., S. J. Taubman, P. D. Brown, M. J. Iacono, and S. A. Clough, 1997: Radiative transfer for inhomogeneous atmospheres: RRTM, a validated correlated-*k* model for the longwave. *J. Geophys. Res.*, **102** (D14), 16 663–16 682, doi:10.1029/97JD00237.

Rotunno, R., and K. A. Emanuel, 1987: An air–sea interaction theory for tropical cyclones. Part II: Evolutionary study using a nonhydrostatic axisymmetric numerical model. *J. Atmos. Sci.*, **44**, 542–561, doi:10.1175/1520-0469(1987)044<0542:AAITFT>2.0.CO;2.

Seifert, A., and K. D. Beheng, 2006: A two-moment cloud microphysics parameterization for mixed-phase clouds. Part I: Model description. *Meteor. Atmos. Phys.*, **92**, 45–66, doi:10.1007/s00703-005-0112-4.

Shapiro, L. J., and H. E. Willoughby, 1982: The response of balanced hurricanes to local sources of heat and momentum. *J. Atmos. Sci.*, **39**, 378–394, doi:10.1175/1520-0469(1982)039<0378:TROBHT>2.0.CO;2.

Skamarock, W. C., J. B. Klemp, J. Dudhia, D. O. Gill, D. M. Barker, and W. Wang, 2007: A description of the Advanced Research WRF version 2. NCAR Tech. Note NCAR/TN-468+STR, 88 pp, doi:10.5065/D6DZ069T.

——, ——, M. G. Duda, L. D. Fowler, S.-H. Park, and T. D. Ringler, 2012: A multiscale nonhydrostatic atmospheric model using centroidal Voronoi tesselations and C-grid staggering. *Mon. Wea. Rev.*, **140**, 3090–3105, doi:10.1175/MWR-D-11-00215.1.

Stensrud, D. J., 2007: *Parameterization Schemes: Keys to Understanding Numerical Weather Prediction Models.* Cambridge University Press, 488 pp.

Stephens, G., 1978: Radiation profiles in extended water clouds. II: Parameterization schemes. *J. Atmos. Sci.*, **35**, 2123–2132, doi:10.1175/1520-0469(1978)035<2123:RPIEWC>2.0.CO;2.

Stern, D. P., and D. S. Nolan, 2012: On the height of the warm core in tropical cyclones. *J. Atmos. Sci.*, **69**, 1657–1680, doi:10.1175/JAS-D-11-010.1.

Straka, J. M., 2009: *Cloud and Precipitation Microphysics: Principles and Parameterizations.* Cambridge University Press, 406 pp.

Tao, W.-K., J. J. Shi, S. S. Chen, S. Lang, P.-L. Lin, S.-Y. Hong, C. Peters-Lidard, and A. Hou, 2011: The impact of microphysical schemes on hurricane intensity and track. *Asia-Pac. J. Atmos. Sci.*, **47**, 1–16, doi:10.1007/s13143-011-1001-z.

Thompson, G., P. R. Field, R. M. Rasmussen, and W. D. Hall, 2008: Explicit forecasts of winter precipitation using an improved bulk microphysics scheme. Part II: Implementation of a new snow parameterization. *Mon. Wea. Rev.*, **136**, 5095–5115, doi:10.1175/2008MWR2387.1.

Tripoli, G. J., and W. R. Cotton, 1980: A numerical investigation of several factors contributing to the observed variable intensity of deep convection over south Florida. *J. Appl. Meteor.*, **19**, 1037–1063, doi:10.1175/1520-0450(1980)019<1037:ANIOSF>2.0.CO;2.

Wang, Y., 2002: An explicit simulation of tropical cyclones with a triply nested movable mesh primitive equation model: TCM3. Part II: Model refinements and sensitivity to cloud microphysics parameterization. *Mon. Wea. Rev.*, **130**, 3022–3036, doi:10.1175/1520-0493(2002)130<3022:AESOTC>2.0.CO;2.

Willis, P. T., 1984: Functional fits to some observed drop size distributions and parameterization of rain. *J. Atmos. Sci.*, **41**, 1648–1661, doi:10.1175/1520-0469(1984)041<1648:FFTSOD>2.0.CO;2.

Willoughby, H. E., F. D. Marks, and R. J. Feinberg, 1984: Stationary and moving convective bands in hurricanes. *J. Atmos. Sci.*, **41**, 3189–3211, doi:10.1175/1520-0469(1984)041<3189:SAMCBI>2.0.CO;2.

——, W. R. Darling, and M. E. Rahn, 2006: Parametric representation of the primary hurricane vortex. Part II: A new family of sectionally continuous profiles. *Mon. Wea. Rev.*, **134**, 1102–1120, doi:10.1175/MWR3106.1.

Wu, L., and B. Wang, 2000: A potential vorticity tendency diagnostic approach for tropical cyclone motion. *Mon. Wea. Rev.*, **128**, 1899–1911, doi:10.1175/1520-0493(2000)128<1899:APVTDA>2.0.CO;2.

Yanai, M., 1958: On the changes in thermal and wind structure in a decaying typhoon. *J. Meteor. Soc. Japan*, **36**, 141–155.

——, 1961a: A detailed analysis of typhoon formation. *J. Meteor. Soc. Japan*, **39**, 187–214.

——, 1961b: Dynamical aspects of typhoon formation. *J. Meteor. Soc. Japan*, **39**, 282–309.

——, 1963a: A comment on the creation of warm core in incipient tropical cyclone. *J. Meteor. Soc. Japan*, **41**, 183–187.

——, 1963b: A preliminary survey of large-scale disturbances over the tropical Pacific region. *Geofis. Int.*, **3**, 73–84.

——, 1964: Formation of tropical cyclones. *Rev. Geophys.*, **2**, 367–414, doi:10.1029/RG002i002p00367.

Zhu, T., and D.-L. Zhang, 2006: Numerical simulation of hurricane Bonnie (1998). Part II: Sensitivity to varying cloud microphysical processes. *J. Atmos. Sci.*, **63**, 109–126, doi:10.1175/JAS3599.1.

Ziegler, C. L., 1985: Retrieval of thermal and microphysical variables in observed convective storms. Part 1: Model development and preliminary testing. *J. Atmos. Sci.*, **42**, 1487–1509, doi:10.1175/1520-0469(1985)042<1487:ROTAMV>2.0.CO;2.